UNIVERSITY OF CAPE COAST

A FIBRE OPTICAL SYSTEM FOR REFLECTANCE

MEASUREMENT OF PLANE SURFACES

BY

SHIELA ESSON

THESIS SUBMITTED TO THE DEPARTMENT OF PHYSICS,

SCHOOL OF PHYSICAL SCIENCES, UNIVERSITY OF CAPE COAST, IN

PARTIAL FULFILLMENT OF THE REQUIREMENTS FOR AWARD OF

MASTER OF PHILOSOPHY DEGREE IN PHYSICS.

MARCH 2011

DECLARATION

Candidate's Declaration

I hereby declare that this is the result of my own original research and that no part of it has been presented for another degree in this University or elsewhere.

…………………………   ………………………

Shiela Esson   Date

(Candidate)

Supervisors' Declaration

We hereby declare that the preparation and presentation of the thesis we supervised were in accordance with the guidelines on supervision of thesis laid down by the University of Cape Coast.

Date…………………………

Dr. Moses Jojo Eghan

(Principal supervisor)

………………………………   Date …………………….

Mr. Ebenezer Teye Tatchie

(Co-Supervisor)

ABSTRACT

A simple fibre optical design for reflectance measurements of plane surfaces has been developed and tested. The reflectance system was standardized with a PF10-03-P01-Plane mirror. Average reflectance from the plane mirror was 99.7%, 99.5% and 70.0% for the 1310 nm, 850 nm LED sources and 632.8 nm He-Ne laser respectively. Average reflectance decreased with decreasing wavelength. Steel and aluminium metal plates showed different trends in average reflectance values. The microscope slide and glass block depicted similar trends as compared to the plane mirror. Surface scans recorded showed variations in reflected intensity, which depicts irregularities on the surface. It was observed that reflectance of the Sony 700 MB CD-R was higher than the CD-WR samples and also it revealed that reflectance decreased abruptly at the boundary between a data recorded section and a non-data section on both CDs. Reflectance for new and expired pharmaceutical tablets showed great variance. The values for new tablets were on average, about 18% higher than for expired tablets. The general results also showed that light intensity depends on the varied longitudinal displacement of the samples as intensity falls off by $1/e^2$. There is the suitability of the reflectance design to be used for quality control as reflectance is a unique property of any material. The optical design is reliable and versatile and can be adapted to quality controlled systems.

ACKNOWLEDGEMENTS

DEDICATION

This thesis is dedicated to my mother Josephine, my husband, Stephen and my sons, Mishael and Rhema.

TABLE OF CONTENTS

Content	Page

CHAPTER FOUR

CHAPTER FIVE

LIST OF TABLES

LIST OF FIGURES

LIST OF PLATES

CHAPTER ONE

INTRODUCTION

Reflection

When light beam is incident on an interface between two different media such as air and glass, most of the light is always scattered backwards and this phenomenon is referred to as reflection (Hecht, 1989). This causes a change in the direction of wavefront at the interface between the two different media and the wavefront returns into the medium from which it originated. This behaviour or wave phenomenon upon interaction with an interface or surface can be demonstrated with electromagnetic waves in the form of light, sound and water waves. The law of reflection says that for specular reflection, the angle at which the light is incident on the surface equals the angle at which it is reflected where the light path is reversible. Specular or regular reflection as seen in figure 1 is the mirror-like reflection of light from a surface, in which light from a single incoming direction (incident ray) is reflected into a single outgoing direction (reflected ray).

This is in contrast to diffuse reflection where incoming light is reflected in a broad range of directions due to microscopic irregularities on the interface as is the case in figure 2. One common model for diffuse reflection is Lambertian reflectance, in which the light is reflected with equal luminance (in photometry) or radiance (in radiometry) in all directions (Hecht, 2008).

Whereas regular reflection results in the formation of an image, the reverse is true for diffuse reflection. By projecting an imaginary line perpendicular to the mirror, known as the normal, the angle of incidence θ_i and the angle of reflection θ_r can both be measured.
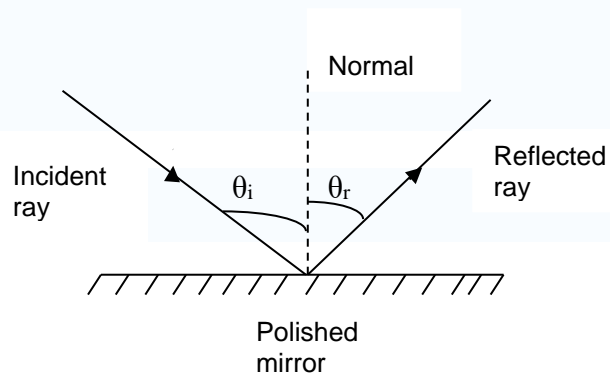
Figure 1: A specular reflection at polished surface
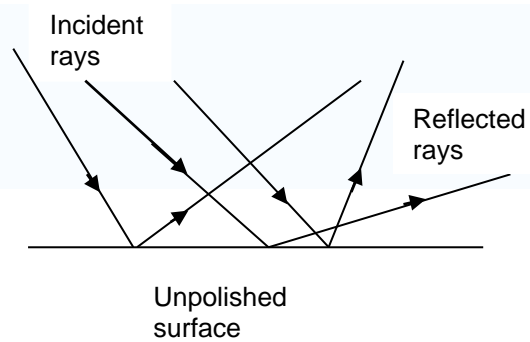
Figure 2: Diffused reflection at an unpolished surface

Surface Reflection

The kind and amount of light reflected from any displayed screen surface depend on the nature of that surface and the angle at which the light incident on it.
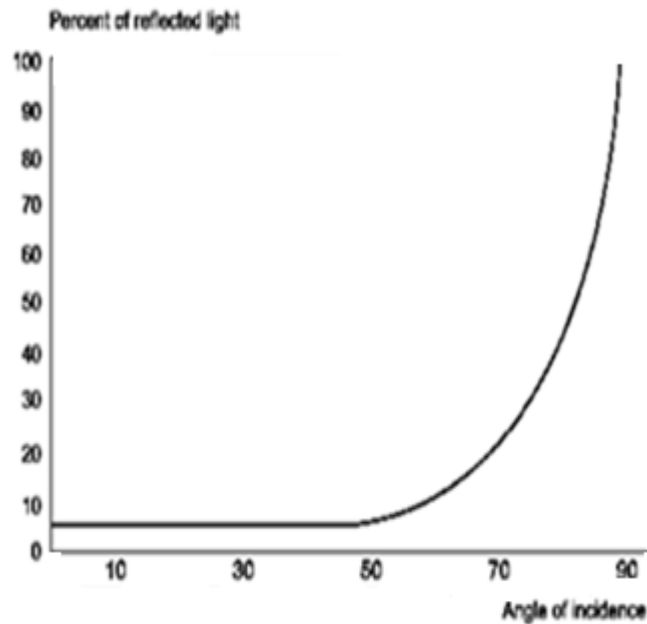
Figure 3: The percent of light beam reflected from a smooth, untreated glass surface as a function of the angle of incidence for air-to-glass surface (Miltcho et al., 2004).

Figure 3 shows that about 4% of the light that incident a smooth, untreated glass surface at an angle of 50° or less is reflected, and that the percentage of light reflection increased as the angle of incidence increases and there is maximum reflection at 90°(normal incidence). Reflection of light depends on the nature of interface present. Thus if the interface is between a dielectric and a conductor, the phase of the reflected wave is retained, otherwise if the interface is between two dielectrics the phase may be retained or inverted depending on the indices of refraction. Reflection from a surface is

characterized by two most important parameters, namely reflectance and reflectivity. Reflectivity measures the fractional amplitude of the reflected electromagnetic field, while reflectance refers to the fraction of incident electromagnetic power that is reflected at an interface. Reflectivity is generally treated as a directional property that is a function of the reflected direction, the incident direction, and the incident wavelength. The reflectance is thus the square of the magnitude of the reflectivity. The reflectivity of a surface can be expressed as a complex number while reflectance always takes a positive or real value. A mirror provides the most common model for specular light reflection, and typically consists of a glass sheet with a metallic coating where the reflection actually occurs. Reflection is enhanced in metals by suppression of wave propagation beyond their skin depths. This is the depth to which electromagnetic radiation or waves can penetrate a conducting surface (Bekefi & Barret, 1977). In transparent material surfaces however, the amount of surface reflection depends on the different refractive indicies between the two materials with regards to wavelength of the light present.

Wavelength-Dependent Effect

The optical properties of materials such as reflection depend on the wavelength of light (Hecht, 2008). The colour of an object is a function of the spectrum of the incident light and the reflectance spectrum of the surface. The choice of a particular paint or ink is aided by the specific colours which they reflect.
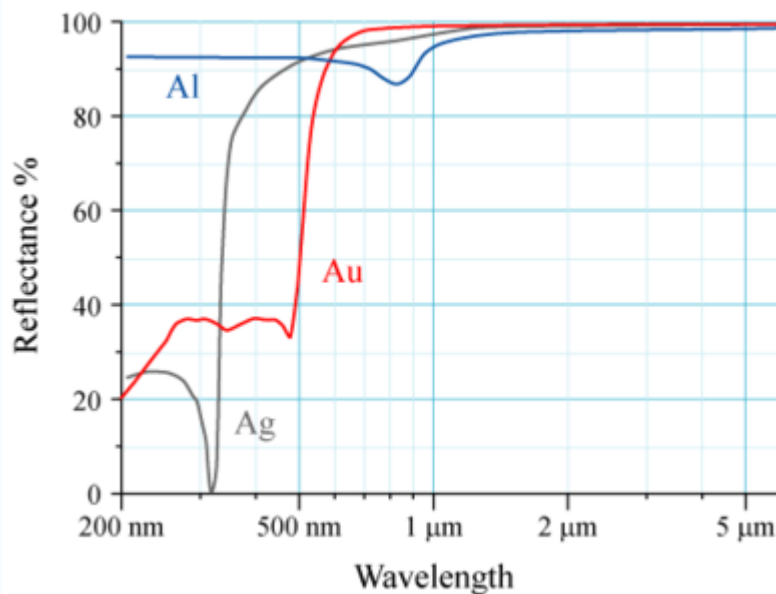
Figure 4:   Spectral reflectance curves for Aluminium (Al), Silver (Ag), and
Gold (Au) metal mirrors at normal incidence (Palais, 1992).

From figure 4, the reflectance spectrum or spectral reflectance curve is the plot of the reflectivity as a function of wavelength and it could be observed that reflectance depends on the wavelength of the incident light. For example, aluminium coated-mirror which is the most common metal amongst the three used for most industrial purposes has the best of reflectivity in the visible region whereas gold and silver reflected well in the infrared regions. Within the optical window, 633 nm to 1300 nm, reflectivity is highly appreciable in

5

all metals and most reflecting surfaces. Reflection also occurs at the surface of transparent media such as glass. The quantum interpretation is that when light waves incident on a material, induces small oscillations in the individual atoms causing each atom to radiate a weak secondary wave (in all directions). All of these waves add up to give the resulting reflection. The phenomenon of reflection is therefore inevitably important as its application extends from echoes in acoustics; studies of seismic waves in geology to VHF (Very High Frequency) for radio transmission and in all instances directly rely on the surface type of the materials in use.

Surface Texture

Surface types define the physical properties of a material including friction, density, reflectivity, depth of penetration, coating adherence etc (Wang & Kusiak, 2001). The relative specular and diffused components of a reflection of a given surface are determined by the characteristics of that surface on the order of the wavelength of the incident light signal. Surface texture sensing has been the focus of most recent research and a variety of sensing approaches have been examined which includes the most common technique which employs the use of surface profilometer. Surface profilometer (stylus) measures the surface topography electromechanically by moving a sample beneath a diamond-tipped stylus. This instrument measures and records vertical movement during surface scanning which reveals the topographical structure of the surface. One key disadvantage of surface profilometer technique is that it touches the surface it is inspecting, which can lead to contamination, damage or destruction of the part (Rideout, 2009).

Surface texture characteristics include roughness, waviness, flatness, contours and defects. Surface texture can also be measured in terms of fine and coarse aggregate when considering particles. The surface finish or roughness affects several functional attributes of the material and is characterized by such an important parameter as the R_a, relative arithmetic mean roughness also known as the Center Line Average (CLA) which is the average roughness. This is the area between the roughness profile and its mean line, or the integral of the absolute value of the roughness profile height over the evaluation length and root-mean square (RMS) roughness.

Guided Waves in Optical Fibres

An optical fibre (or fibre) is a glass or plastic material that carries light along its length and hence is a medium through which information is carried. They usually consist of an inner core and outer cladding whose refractive indices are different. Light is kept in the core of the optical fibre on a path called a mode by a phenomenon of total internal reflection (TIR) illustrated in figure 5. This causes the fibre to act as a waveguide. Fibres are used instead of metal wires because signals travel along them with less loss, and they are also immune to electromagnetic interference. Fibres which support many propagation paths or transverse modes are called multi-mode fibers (MMF), have a core bigger in diameter and are used for applications where high power must be transmitted. Those which can only support a single guided mode are called single-mode fibres (SMF). Thus, at the operating wavelength, only one specific field distribution can propagate along the fibre with very little attenuation (Ghatak & Shenoy, 1994).

Special connectors are used in connecting and detaching two fibres and this reduces coupling problems. There are also different types of specially designed fibres such as the bifurcated multimode optical fibre usually referred to as the Y-shaped fibre which are used for a variety of applications including reflection based sensing.
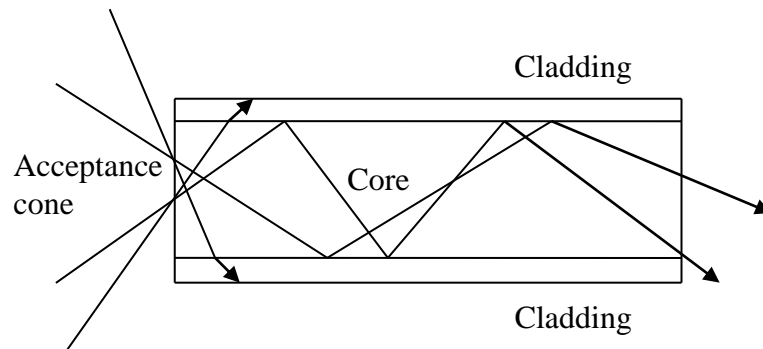
Figure 5: The propagation of light through a multimode optical fibre

demonstrating total internal reflection

Principle of Optical Fibre Sensing

In most, optical fibre sensing, the quantity being measured changes the optical properties of the light in a way that can be detected and measured. For example, the pressure changes induced in a fibre by acoustic waves changes the amount of light transmitted by the fiber (Byrne et al., 1995). Optical fibre sensing consists basically of an optical source whose relevant optical properties remain constant, launched into a fibre transmission line via a stable coupling mechanism to direct the light unto an area (usually an area or surface of interest). The light is then returned after being modified in some way by the sensing interaction, in a reflective mode as illustrated in figure 6, to a photodetector and subsequently to an electronic processing system. In the transmission mode, the direct effect of the environment that surrounds the bare

8

fibre on the light is also detected by a detecting system as shown in figure 7. The signal processing system then detects the changes introduced in the optical signal by the sensing area and then relates this to a change in the measurand field of interest, usually in the form of output intensity (power). The major parameters which influence the detected power are the reflectivity of the surface, the proximity of the sample surface, the angle of incidence of the light and the acceptance angle of the sensing fibre (Boyles, 1994). The sensing technique is therefore the ''Cinderella'' of the information age (Culshaw & Dakin, 1988). The inherent advantages of optical fibre sensing include their being resistant to electromagnetic interference, their small size nature which usually requires low power for its operation and their high sensitivity (Giallorenzi et al., 1982).
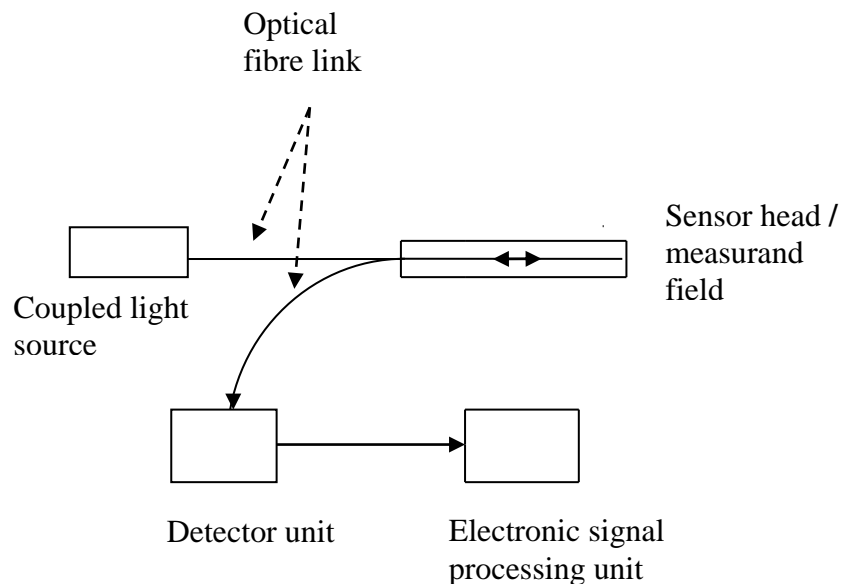
Figure 6: Schematic diagram of a general optical fibre sensor system

operating in the reflective mode

Optical
fibre link

Detector
unit

Coupled light
source
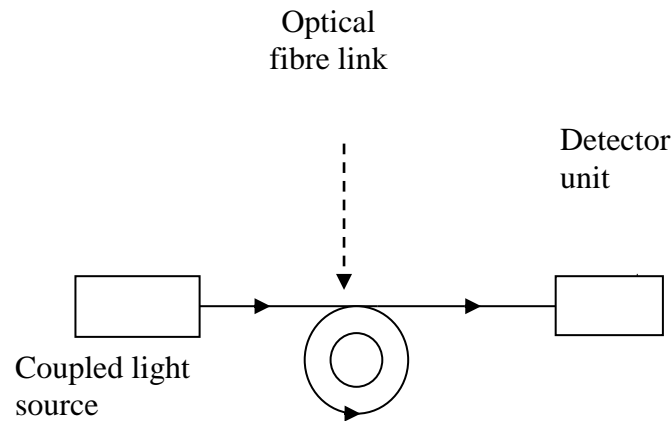
Figure 7:   Schematic diagram of a general optical fibre sensing system

operating in the transmitting mode

Sensing Classification

Sensing area can either be in the form of a point sensor making measurement in a localized area or may be a distributed sensor which has the ability to measure along a length of the optical fibre. There is extrinsic sensor to the fibre and consists of bulk optical component configured into a sensing mechanism, or it may be an intrinsic sensor to the fibre where measurement process takes place within the optical fibre medium. In the former case optical fibre becomes a medium of transmitting the light to and from the sensing area, while in the latter it actively takes part in the sensing process where the inherent optical properties of the fibre are utilized. The operation and choice of an optical fibre sensor purely depend on the application and the measurement method being employed. Thus, extrinsic sensors are those which use fibre to supply light to a sensing device and return (reflect) signal light to a detection system. Sensing systems have their own related operating performance factors which can be identified as those factors that define a

measurement point, which include resolution, responsivity, sensitivity, accuracy and reproducibility (Yeh, 1989).

The fibre for sensing

Many different types of fibres are used as medium for sensing different parameters. The graded index multimode optical fibre is the premier choice for maximizing the amount of power captured from light source in limited distance applications. Its large core and high NA provide excellent coupling efficiency over other fibres. Its varied applications include aerospace, defense and quality control. The bifurcated multimode optical fibre is a two way branched fibre or a Y-shaped assembly that has two fibres of the same diameter side-by-side in the common end, or the tail of the assembly referred to as the sensing area or the fibre probe tip in figure 8. From the nexus or the breakout of the assembly, the two fibres diverge into two arms. It allows light from a source through one arm to interact with an external reflecting surface and come out of the other arm after an inter-mixing of the reflected light and the light from source with less attenuation. Notably, either the input or the output arms could be used interchangeably based on the choice of purpose. There is no clear-cut restriction. Having high sensitivity to short distances, bifurcated optical fibre is well suited for position sensing application, gauging and surface assessment (Culshaw & Darkin, 1988).

Output arm

Fibre probe tip
(sensing area)

Input arm
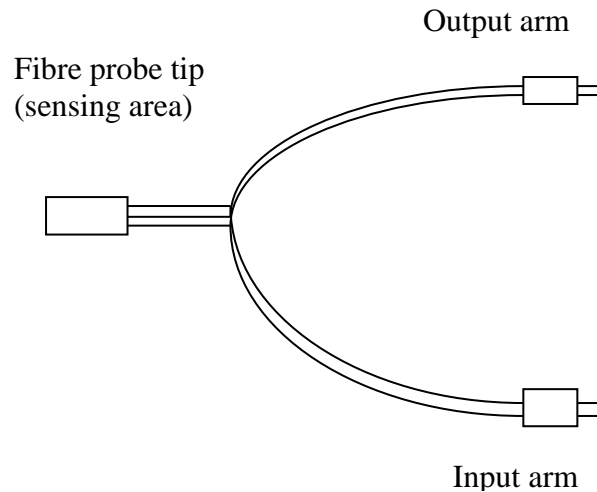
Figure 8:   A sketch of a bifurcated multimode optical fibre probe

Sources and Detectors

Light sources may be light emitting diodes (LED), laser, or broadband sources such as tungsten halogen lamp. The choice of light source depends on the application. In this work the source choice was characterized by the fact that scattering prevails over absorption between 600 nm - 1500 nm. Most importantly, LEDs are more suitable for linear systems than Laser diodes (LDs) because they exhibit a smooth (nearly linear) power/current relationship whereas the LDs exhibit non-linearity.

The PIN photodiode is the most common detector used in optical systems. However, depending on the application and the detector characteristics such as detector sensitivity, active area, linearity, bandwidth, wavelength range of operation, and electrical biasing, a selection may be made. Silicon detectors are widely used in the 0.4 μm -1.0 μm wavelength range while germanium detectors are for measurements in the 0.8 - 1.7 μm range (Ghatak & Shenoy, 1994).

Related Work

Previous research on using fibre optics in surface roughness measurement was performed by Spurgeon and Slater and by Lin (Lin et al., 1977). They used fibre bundles to deliver light to and collected the reflected light from a surface to a detecting system. A correlation was found between the intensity of the reflected light (as measured by the photodetector) and the average roughness of the surface. However, both techniques suffered from changes in the reflected light intensity due to varying reflectance properties of the surface under inspection. Additionally, the measurement lacked sufficient sensitivity and were only suitable for measurements on smooth surface up to R_a of 0.5 μm (Spurgeon & Slater, 1974). North and Agarwal circumvented these problems by using two fibre optic bundles, which illuminated the surface at two angles of incidence. The ratio of the two reflected light intensity removed the problem of surface reflectivity variation (North & Agarwal, 1983). This instrument showed good correlation with stylus measurements up to 1 μm of R_a value. The fibre optic sensing described does not provide any surface profile data: they simply correlate the collected light intensity with the R_a measured by stylus (Bradley & Jeswiet, 1999).

The Scope of This Work

The objective of this research is to design an optical system which seeks to investigate or examine material surfaces based on the interaction between light and the sample surface. Eight different materials were used which included: a (PF10-03-P01) plane mirror, glass block, a microscope slide, polished aluminium plate, a non galvanized steel plate, a CD-

R(recordable compact disc), CD-RW(re-writable compact disc) and some locally manufactured paracetamol tablets. A comparison is made of their surface reflectance. An understanding is explored by using the mirror reflectivity as a standard parameter to evaluate optical sensitivity. The wavelengths of light sources used were He-Ne laser at 632.8 nm, LEDs at 850 nm and 1310 nm respectively.

Arrangement of the thesis

This thesis is organized as follows: chapter one begins with a general overview of surface reflection, the basics of light transmission in the fibre, the fundamental sensing mechanism and basic applications of the sensor. Chapter two discusses the literature review of the concept of surface reflection. This chapter also holds an overview of the various theories and models of light propagation and interaction with matter, the bifurcated optical fibre as well as operation at the detection point. Experimental procedures for the measurement of the intensities of surface reflection of the various samples used are discussed in chapter three. Analysis of experimental results and discussion are contained in chapter four. Chapter five gives the conclusion and recommendations for future work.

CHAPTER TWO

THEORETICAL REVIEW OF LIGHT PROPAGATION AND

INTERACTION WITH MATTER

Light interaction with matter or any object may result in a phenomenon in optics. This phenomenon may include reflection, refraction and transmission. In some cases, scattering or absorption may also occur. Interaction at the surface of the object may result in internal reflection or external reflection. The type of reflection and its characteristics may be strongly influenced by the angle of incidence of the light to the surface, the polarization state of the incident light, as well as the nature of the surface. For the purpose of this work, the focus will be on reflection from some plane surfaces. The light would be considered as waves in which the electromagnetic wave theory could be employed.

Electromagnetic Wave Theory

The dominant property of light is its wave nature and the existence of light as an electromagnetic wave in classical theory was established by the Scot physicist James Clerk Maxwell (1831-1879). He did this by collecting electromagnetic theory into a correlated set of mathematical relationships that justified the hypothesis that light behaved like an electromagnetic wave. This wave equation permitted free space solutions, which corresponded to electromagnetic waves with the velocity equal to the known experimental

value of speed of light. The results confirmed light propagation as an electromagnetic phenomenon, thus making it clearer for its behaviour to be understood (Palais, 1992).

Maxwell's four equations in their differential form (see equations (1) to (4)) treat light as an electromagnetic wave and also portray all the important features of light when carefully examined.

$$\nabla \cdot \overline{E} = \frac{\overline{\rho}}{\varepsilon_0} \tag{1}$$

$$\nabla \cdot \overline{B} = 0 \tag{2}$$

$$\nabla \times \overline{E} - \frac{\partial \overline{B}}{\partial t} \tag{3}$$

$$\nabla \times \overline{B} = \mu_0 \left(\overline{J} + \varepsilon_0 \frac{\partial \overline{E}}{\partial t} \right) \tag{4}$$

where $\overline{E}$ and $\overline{B}$ are macroscopic fields whereas $\overline{\rho}$ is the macroscopic charge density and $\overline{J}$ is the current density. The fields are high-frequency oscillating optical fields and so the response of electrons and ions are also considered at such high frequencies. This is an essential consideration since the parameters of a material are a function of the optical frequency (Guenther, 1990).

For a Cartesian axes (as seen in figure 9), a typical sinusoidal solution is given by

$$E = E_o exp\{i(\omega t - kz)\} \tag{5}$$
$$B = B_o exp\{i(\omega t - kz)\}$$
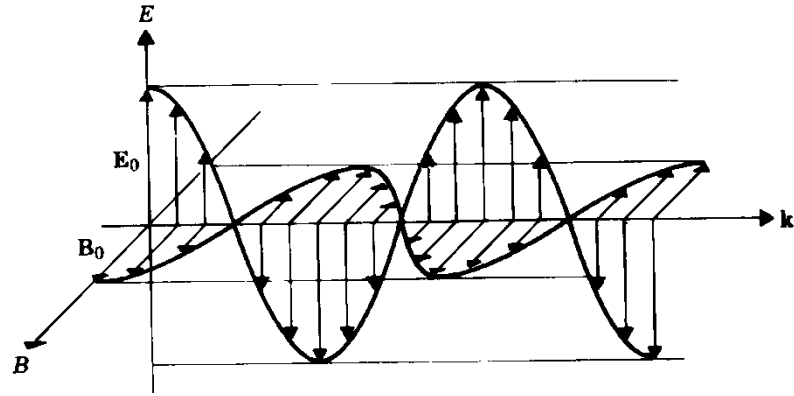
Figure 9: Electromagnetic field patterns in a plane wave at a fixed

point (Guenther, 1990).

which states that the magnetic field B oscillates orthogonally to the electric

field E and is in phase also with the electric field. The wave propagation is in

the direction of $\mathbf{k}$. The frequency, v and wavelength, λ of the wave are given

by

$$v = \omega/2\pi$$

$$\lambda = 2\pi/k$$

and $v\lambda = \omega / k = c$ where c is the wave velocity, k is the wave number. This

was a complementary law which was later introduced by Maxwell and it

relates to the electromagnetic properties of the medium in which the wave

propagates via the equation

$$c = (\mu\varepsilon)^{-1/2} \tag{6}$$

where ε and μ are the electric permittivity of the medium and its magnetic

permeability respectively. The coefficient of the amplitudes E_o and B_o

(strength of the respective fields) in equation (6) is also referred to as the

wave impedance of the medium. Maxwell's equations hold for the electric

displacement D and the magnetic flux density but only differ from free-space quantities by the following substitutions

$$\varepsilon_o \rightarrow \varepsilon$$

and

$$\mu_o \rightarrow \mu$$

The constants $\mu_o \, \varepsilon_o$ are the permeability and permittivity of free space. The wave equation for the vector fields E and B is found by using the identity (Adams, 1981).

$$\text{curl curl} = \text{grad div} - \nabla^2 \tag{7}$$

The electromagnetic properties of the medium in which the wave propagates is related to the velocity of light in free space c as

$$c = \left(\frac{1}{\varepsilon_o \mu_o}\right)^{\frac{1}{2}} \tag{8}$$

Relation (8) can be written in the form

$$c = \left(\frac{1}{\varepsilon_o \mu_o \varepsilon_R \mu_R}\right)^{1/2}$$

We can therefore as well write

$$c = \frac{c_o}{\varepsilon_o \mu_R} \tag{9}$$

where, c_0 is the velocity of the electromagnetic wave in free space and has the experimentally determined value 2.997925×10^8 ms^{-1}. Most dielectric materials have $\mu_R \approx 1$ and $\varepsilon_R > 1$ and are often used as electrical insulators. Thus we can write equation (9) in the form

$$c = \frac{c_o}{(\varepsilon_R)^{1/2}} \tag{10}$$

And when $c < c_0$, the ratio $^c/_{c_0}$ is by definition the refractive index n of the medium and we have

$$n = \varepsilon_R^{1/2} \tag{11}$$

Now ε_R is a measure of the ease with which the medium can be polarized electrically by the action of an external electric field. This polarization depends on the mobility of the electrons within the molecule in the face of resistance by molecular force. Clearly then, ε_R will depend on the frequency of the applied electric field since it will depend on how quickly these forces respond. Thus equation (11) will be true only if n and ε_R refers to the same wave frequency, and that n is also frequency dependent. The parameters ε_R and μ_R are the relative permittivity and relative permeability factors respectively of the medium relative to those for free space, ε_o and μ_o (Culshaw & Dakin, 1988).

Another essential solution is that of a wave which spreads from a point spherically (Gaussian distribution) given by

$$E_r = \frac{E_0}{r} exp\{i(\omega t - k.r)\} \tag{12a}$$

Here, the factor of $\frac{1}{r}$ in the amplitude is necessary to ensure energy conservation, for the total area over which the energy flux occurs is $4\pi r^2$ so that the intensity drops as $\frac{1}{r^2}$ since intensity is directly proportional to the square of the amplitude.

The electromagnetic theory leads to the following expression for the energy density (in SI units) associated with electric and magnetic fields in free space: (Smith & Thompson, 1988).

$$\boldsymbol{U} = \frac{1}{2}\left[\varepsilon_0 \boldsymbol{E} \cdot \boldsymbol{E} + \frac{1}{\mu_0}\boldsymbol{B} \cdot \boldsymbol{B}\right] \tag{12b}$$

From the theory,

$$B.B = \frac{1}{c^2}E \cdot E = \varepsilon_0\mu_0 E \cdot E \tag{13}$$

So by substituting, equation (13) into (12b), the resulting equation becomes:

$$U = \varepsilon_0 E \cdot E = \varepsilon_0|E|^2 \tag{14}$$

The energy flow per unit area of a surface, or energy flux density, in the direction of propagation is defined by the poynting vector (Furtak & Klein, 1986).

$$S = \frac{1}{\mu_0}E \times B \tag{15}$$

This important vector gives the energy flux density or irradiance in an arbitrary direction (that which is identified by the unit vector η) by means of the scalar product $\eta.S$ as seen in figure 10. That is:

$$|S|_{surface} = \eta \cdot S = S\cos\theta$$
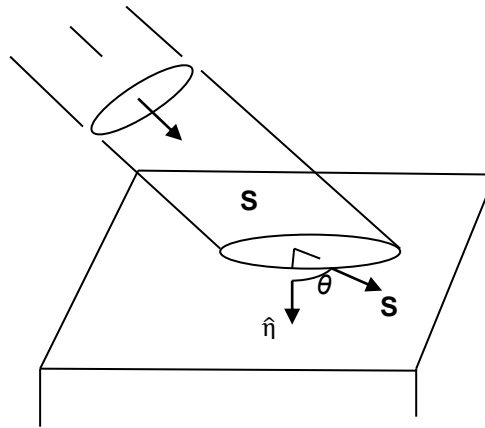
Figure 10: The energy flux density on a surface which depends on the angle of incidence

Since $\mathbf{S}$ or $\mathbf{U}$ will involve terms quadratic in $\mathbf{E}$ it is necessary for the real form of $\mathbf{E}$ to be considered. For linearly polarized plane waves in vacuum, we have the following expressions for real physical fields (Furtak & Klein, 1986).

$$\mathbf{E} = \mathbf{E_0} \cos \emptyset \quad \text{where, } \emptyset = \omega t - k.r + \varphi \tag{16}$$

$$\mathbf{B} = \mathbf{B_0} \cos\emptyset = \frac{k.E_0}{ck} \cos \emptyset \tag{17}$$

here, r and φ denote position vector of a point in the plane and phase difference respectively. Hence, $\mathbf{S}$ is given by

$$\mathbf{S} = \frac{1}{\mu_0} E_0 \frac{(k \cdot E_0)}{ck} \cos^2 \emptyset = \varepsilon_0\, c |\mathbf{E_0}|^2 s\cos^2\emptyset \tag{18}$$

The time average value of the magnitude of the poynting vector $\langle \mathbf{S} \rangle$ is therefore given by

$$\langle \mathbf{S} \rangle = \frac{\varepsilon_0 c}{2} |\mathbf{E_0}|^2 \cos^2\emptyset \tag{19}$$

where $\cos^2(\omega t - k.r + \varphi) = 1/2$ and is a measure of the irradiance I Thus,

$$\langle \mathbf{S} \rangle = c^2 \varepsilon_o |\mathbf{E} \times \mathbf{B} : \quad \langle \cos^2(\omega t - k.r + \varphi) \rangle \tag{20}$$

which makes equation (20) become (21)

$$\langle \mathbf{S} \rangle = \frac{c^2 \varepsilon_o}{2} |\mathbf{E} \times \mathbf{B}| \tag{21}$$

and hence

$$I = \langle \mathbf{S} \rangle = \frac{c^2 \varepsilon_o}{2} \mathbf{E^2} \tag{22}$$

This quantity is the irradiance and is what our eyes or any detector would be sensitive to. The time-averaged energy flow is along the wave vector k, in the direction of propagation of the wave (Hecht, 1989). It is therefore known in the case of light waves that the square of the amplitude of the wave at a point is proportional to the intensity of light.

For a wave in a vacuum, the energy density is given from equation (12) by

$$U = \varepsilon_0 |E_0|^2 cos^2\emptyset \tag{23}$$

with a time average of

$$\langle U \rangle = \frac{\varepsilon_0}{2} |E|^2 \tag{24}$$

This is a general result

Energy flux density = (energy density) x (propagation speed)

Light wave Fundamentals

The problem regarding the amount of light reflected at a boundary between two dielectrics is an important part of the study of optics. These problems are particularly critical in the design and analysis of optical systems. In the 16th century, the laws of reflection and refraction were first formulated in terms of ray of light. A light ray incident upon a reflective surface will be reflected at an angle equal to the incident angle. Both angles are typically measured with respect to the normal to the surface. The law of reflection can be derived from Fermat's principle.

Fermat's principle for reflection

Fermat's principle is of the view that light follows the path of least time. The law of reflection can be derived from this principle (shown in figure 3) as follows:
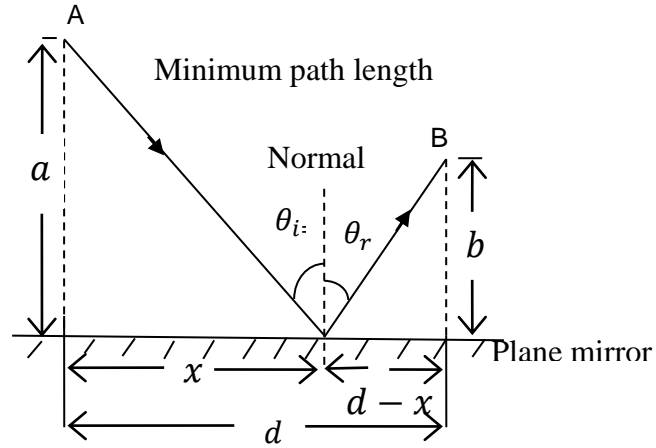
Figure 11: Geometric representation of reflection showing the minimum

pathlength between points A and B for the derivation of the law of

reflection

Considering a path length L from A to B it is possible to deduce equation (25)

$$L = \sqrt{a^2 + x^2} + \sqrt{b^2 + (d-x)^2} \qquad (25)$$

At constant time, the minimum path is considered as the minimum distance

traveled by the light. This is found by setting the derivative of L with respect

to x to zero.

$$\frac{dL}{dx} = \frac{1}{2}\frac{2x}{\sqrt{a^2+x^2}} - \frac{1}{2}\frac{2(d-x)}{\sqrt{b^2+(d-x)^2}} = 0 \qquad (26)$$

This reduces to equation (27) and by using Pythagoras theorem from figure11,

$$\frac{x}{\sqrt{a^2+x^2}} = \frac{(d-x)}{\sqrt{b^2+(d-x)^2}} \qquad (27)$$

The left and right side of equation (27) become $\sin\theta_i$ and $\sin\theta_r$ respectively

resulting in equation (28)

$$\sin\theta_i = \sin\theta_r \qquad (28)$$

and subsequently for small angle approximations,

$$\theta_i = \theta_r \qquad (29)$$

The law of reflection (equation (29)) justifies the same reflected image produced in a plane mirror where the virtual image distance behind the mirror is the same as the object distance in front of the mirror (Jerkins & White, 1995).

The basis of geometric or ray optics relies on this law most essentially. The law however has limitations such as it inability to be used in predicting reflected intensities. Wave theory may appear complex in the context of light propagation. However, in dealing with the phenomenon of reflection the ray theory is simple and may only convert a wave into a group of rays in the direction of propagation of light normal to a surface whose phase is constant and obey simple geometric rules (Liu et al., 2001).

Therefore reflection occurs because certain surfaces have the property of reflecting or returning rays of light, which fall upon them, according to the defined law. This may occur in the situation of the air to glass boundary where light is coupled from a source into a fibre, and the sun's ray hitting the surface of a clear water body etc. Any object surface which reflects light is called a reflector.

$$n_1 \qquad n_2$$

Incident beam ⟹ ⟸ ⟹ Transmitted beam

↗

Reflected beam
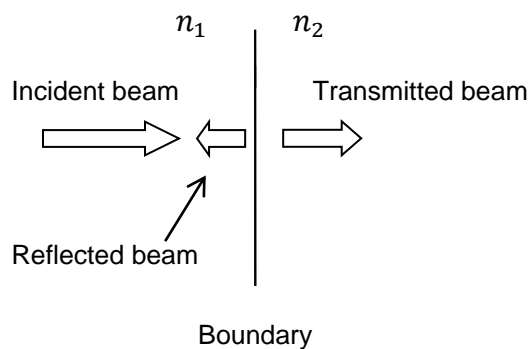
Boundary

Figure 12: A wave incident on a plane boundary between two dielectrics

(refractive indicies n_2 and n_1) at normal incidence

The simplest computations for reflection are those for which the incident beam is travelling normal to the boundary, as in figure 12. The reflection coefficient ρ is the ratio of the reflected electric field to the incident electric field. The reflectance R is therefore the ratio of the reflected beam intensity to the incident beam intensity and since intensity in an optical beam is proportional to the square of its electric field, reflectance can be expressed as the square of the reflection coefficient. Thus

$$R = \rho^2 \tag{30}$$

By computation, the reflectance for an air-to-glass interface is 0.04 so that 4% of light is reflected.

Fresnel Reflection

The mathematical description for the behavior of light when moving between media of different refractive indices was deduced by Augustin-Jean Fresnel. He gave conditions to formulate equations which predict the reflection of light at a boundary. When light moves from a medium of a given refractive index n_1 to a second medium with refractive index n_2, both reflection and refraction (transmission) of the light may partially occur (Smith & Thompson, 1988).
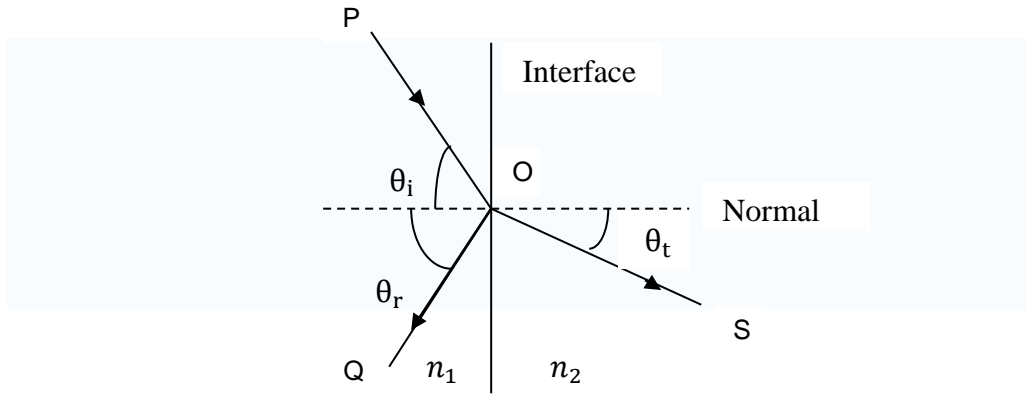
Figure 13:   Geometry of reflection and refraction at a plane interface

In figure 13, an incident light ray PO strikes at point O the interface between two media of refractive indexes n_1 and n_2. Part of the ray is reflected as ray OQ and part refracted as ray OS. The angles that the incident, reflected and refracted rays make to the normal of the interface are given as θ_i , θ_r and θ_t respectively. The relationship between these angles is given by the law of reflection and Snell's law. The fraction of the incident power that is reflected from the interface is given by the reflectance R and the fraction that is refracted is given by the transmittance T. Assuming the media to be non-magnetic, the calculations of R and T depend on polarization of the incident ray. If the light is polarized with the electric field of the light perpendicular to the plane as shown in figure 13, then it is said to be s-polarized and the reflection coefficient is given by:

$$R_s = \left[\frac{\sin(\theta_t - \theta_i)}{\sin(\theta_t + \theta_i)}\right]^2 = \left(\frac{n_1\cos\theta_i - n_2\cos\theta_t}{n_1\cos\theta_i + n_2\cos\theta_t}\right)^2$$

$$= \left[\frac{n_1\cos\theta_i - n_2\sqrt{1-\left(\frac{n_1}{n_2}\sin\theta_i\right)^2}}{n_1\cos\theta_i + n_2\sqrt{1-\left(\frac{n_1}{n_2}\sin\theta_i\right)^2}}\right]^2 \quad (31)$$

where θ_t can be derived from θ_i by Snell's law and is simplified by using trigonometric identities. If the incident light is polarized in the plane of the diagram which is p-polarization, then R is given by:

$$R_p = \left[\frac{\tan(\theta_t - \theta_i)}{\tan(\theta_t + \theta_i)}\right]^2 = \left(\frac{n_1\cos\theta_t - n_2\cos\theta_i}{n_1\cos\theta_t + n_2\cos\theta_i}\right)^2$$

$$= \left[\frac{n_1\sqrt{1-\left(\frac{n_1}{n_2}\sin\theta_i\right)^2} - n_2\cos\theta_i}{n_1\sqrt{1-\left(\frac{n_1}{n_2}\sin\theta_i\right)^2} + n_2\cos\theta_i}\right]^2 \quad (32)$$

If the incident light is unpolarized (containing an equal mix of s- and p- polarizations), the reflection coefficient is $R = (R_s + R_p)/2$. Equations for coefficients corresponding to ratios of the electric field amplitudes (*r, t*) of the waves can also be derived, and these are also called Fresnel equations. These can be represented in several forms, depending on the choice of formalism and sign-convention used.

At one particular angle for a given n_1 and n_2, the value of R_p goes to zero and a p-polarized incident ray is purely refracted. This angle is known as Brewster's angle (in figure 14(a)), and is around 56° for a glass medium in air or vacuum. This statement is only true when the refractive indexes of both materials are real numbers, as is the case for materials like air and glass. For materials that absorb light, like metals and semiconductors, n is complex, and

R_p does not generally go to zero. When light moves from a denser medium into a less dense one (i.e., $n_1 > n_2$), and the incidence angle is greater than an angle known as the critical angle (in figure 14(b)), all light is reflected and R_s and R_p are equal and thus

$$R_s = R_p = 1 \tag{33}$$

This phenomenon is known as total internal reflection (with its range depicted in figure 14 (b)) and the critical angle is approximately $41°$ for glass in air. (Tyndall, 1854).

(a)   (b)
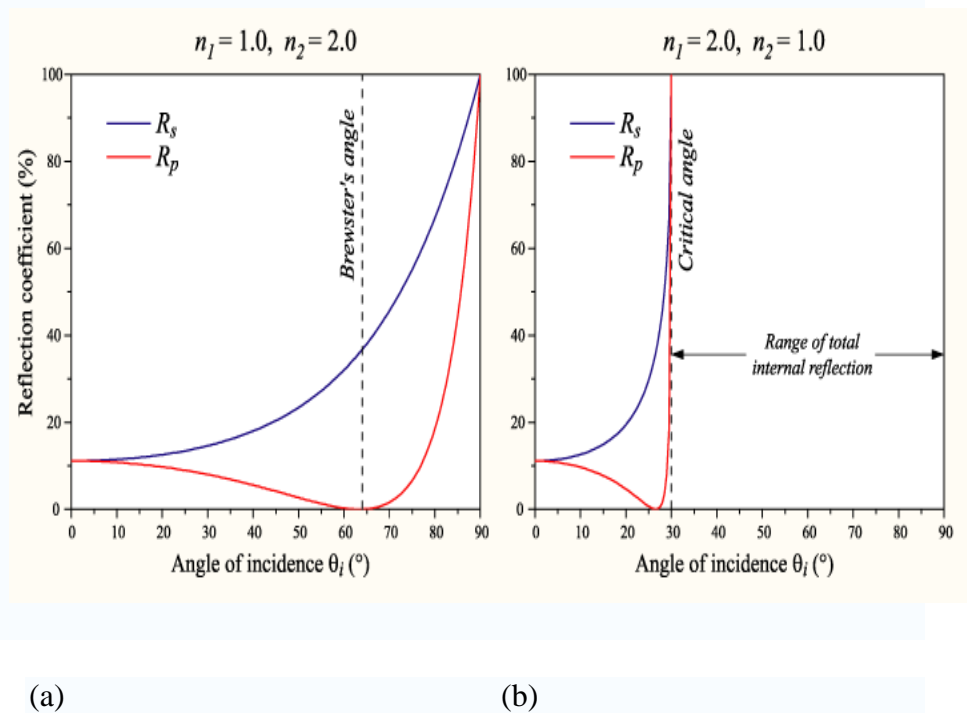
Figure 14: (a) Graphical representation of Brewster's angle and (b) the range of total internal reflection for reflections at an air-to-glass and glass-to-air interface (Smith & Thompson, 1988).

When the light is at near-normal incidence to the interface $(\theta_i \approx \theta_t \approx 0)$, the reflection R and transmission T coefficients are respectively given by:

$$R = R_s = R_p \tag{32}$$

$$T = T_s = T_p = 1 - R = \frac{4n_1 n_2}{(n_1 + n_2)^2} \tag{33}$$

For normal incidence, the reflectance ρ is given by:

$$\rho = \frac{n_1 - n_2}{n_1 + n_2} \tag{34}$$

where, n_1 is the refractive index in the incident region and n_2 is that of the transmitted region. If $n_2 > n_1$, then the reflection coefficient becomes negative. This is said to indicate a 180° phase shift between the incident and the reflected electric fields.

The reflection by a glass window is from the front side as well as the back side and that some of the light is reflected a number of times between the two sides. The combined reflection coefficient for this case is *2R/ (1 + R)*, when interference is neglected with the assumption that the permeability μ is equal to vacuum permeability μ_0 in both media (Hecht, 1987). This is approximately true for most dielectric materials, but not for some other types of materials. Reflectance does not vary a great deal for incident angles near zero. For certain incident angles and polarization states the zero reflectance means full transmission. Total reflection occurs when reflectance is unity for a range of incident angles (Palais, 1992).

Theories of the bifurcated fibre probe tip.

The bifurcated fibre tip in front of a mirror is considered to be a set of two independent parallel ends contacting each other with no space left between them. Both the transmitting (input arm) and receiving (output arm) ends have perfectly circular cross sections with area S_a and radius w_a as shown in figure 15. The light leaving the transmitting end is represented by a perfectly symmetrical cone with divergence angle θ_a and vertex O located at a distance z_a inside the arm, as shown in figure 16. The amount of light returning to the detector depends on the distance h between the fibre probe tip and the surface being monitored.
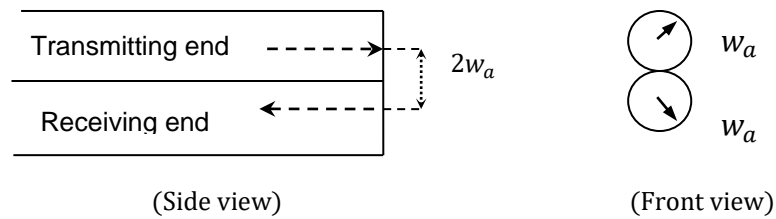
Figure 15: Lateral and frontal view of the transmitting and receiving ends of

the fibre probe tip
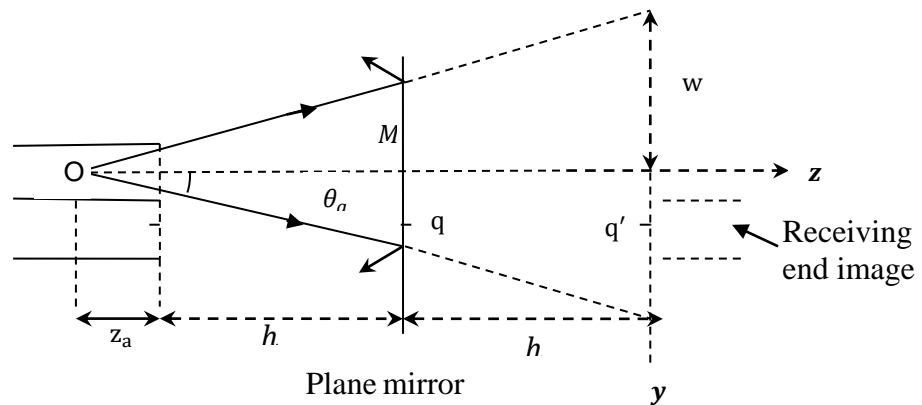
Figure 16: The cone of light exiting the transmitting end of the fibre tip

30

By extending the virtual incident cone of light beyond the mirror, so that the z-coordinate is aligned with the emitted light cone axis beginning at O and extending beyond the mirror surface. Following the representation in Figure 16, the coordinates of the center point q' in the receiving end are coordinates of equation (35) where h is the distance under consideration which in this work is referred to as the longitudinal displacement.

$$q' \begin{cases} y = 2w_a \\ z = z_a + 2h \end{cases} \tag{35}$$

Geometrically, assuming that the light intensity (irradiance) is constant for all points with the same z-coordinates inside the circular cross section of the cone and that there is no intensity outside of the cone, then

$$z > z_a = \begin{cases} \text{Inside the cone } I(z) = \frac{P_E}{\pi w^2(z)} \\ \text{outside the cone } I(z) = 0 \end{cases} \tag{36}$$

where P_E is the optical power emitted by the transmitting fibre end and w is the cross section of the cone for the z-coordinate (current). Thus,

$$w(z) = z\tan\theta_a = z\frac{w_a}{z_a} \tag{37}$$

The optical power collected at the tip of the receiving end may be obtained by evaluating the overlapping area of the circle of radius $w(z)$ corresponding to the emitted light cone and the circle of radius w_a corresponding to the collecting area of the receiving end. If centers of both circles are separated by $2w_a$, then in evaluating the overlapping area two different cases can be taken into account as depicted in figure 17. The first case is considered for small values of h where the receiving end is partially illuminated and secondly when the receiving end is completely illuminated occurring at larger values of h and

are respectively represented in figures 17(a) and (b). When $h < z_a$ or $w(z) <$ $3w_a$ occurring in figure 17(a), simple algebra involving triangle equations and trigonometric functions are used to determine the overlapping area as:

$$S(z) = w^2(z)\alpha_1(z) + w_a{}^2[\alpha_2(z) - \sin\alpha_2(z)]$$

$$-w_a w(z)\sin\alpha_1(z) \qquad (38)$$

where α_1 and α_2 are angles which can be evaluated through equation (39).

$$\alpha_1(z) = arccos\left\{\frac{w(z)}{4w_a} + \frac{3w_a}{4w(z)}\right\} \qquad (39a)$$

and

$$\alpha_2(z) = arccos\left\{\frac{5}{4} - \left[\frac{w(z)}{2w_a}\right]^2\right\} \qquad (39b)$$

(a)   (b)
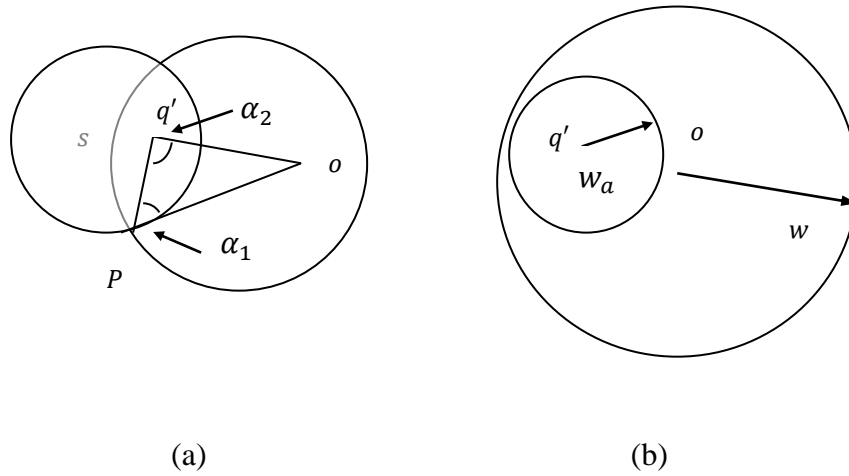
Figure 17: Diagrams of circles representing (a) partial illumination

(h $< z_a$) and (b) total illumination for h $\geq z_a$

In figure 17, the large circle of radius w represents the z-cross section of the light cone. The small circle of radius w_a represents the receiving end surface where $2w_a = oq'$, $Pq' = w_a$ and $oP = w$.

The power collected by the receiving fibre end is obtained by multiplying the illuminated area S by the light irradiance in equation (36). That is,

$P(z) = \int_S I(z)ds = I(s)s(z)$ to give equation (41):

$$P(z) = P_E \frac{S(z)}{\pi w^2(z)} \qquad (41)$$

The received optical power is the product of the collecting surface area (S) $\pi w_a{}^2$ by the irradiance $I(z)$. The irradiance of the emitted light does not remain constant over beam cross-sections, but rather decreases radially obeying an exponential law (Siegman, 1989). Therefore, in the case of total illumination that is $h \geq z_a$ or $w(z) < 3w_a$, we obtain equation (42).

$$P(z) = P_E \frac{w_a{}^2}{w^2(z)} \qquad (42)$$

Equation (43) gives a summary of the two conditions as follows:

$$\begin{cases} for\ 0 \leq h < z_a; \\ P(z) = \left\{ \frac{P_E}{(z)} \frac{1}{\pi} \alpha_2(z) - \sin\alpha_2(z) + \zeta(z)[\alpha_1(z)\zeta(z) - \sin\alpha_1(z)] \right\} \\ for\ h \geq z_a;\ \frac{P_E}{\zeta^2(z)} \end{cases} \qquad (43)$$

The dimensionless parameter ζ is dependent on the radius $w(z)$ and the distance h given by

$$\zeta = w(z)\frac{1}{w_a} = 1 + \frac{2h}{z_a} = 1 + 2h_N \qquad (44)$$

The plot of normalized collected power $P_N = \frac{P}{P_{max}}$ versus the normalized

$h_N = \frac{h}{z_a}$ distance shows that power increases from zero to the maximum for

small values of h and power falls off according to $\frac{1}{\zeta^2}$ law of values for h

higher than z_a (as in figure 18). However, working within an effective distance h, an approximate value of about 1.0 from a surface, a characteristic curve can be displayed with a sketch as in figure 19(a) where maximum power occurs just before the receiving probe tip gets totally inside the light cone. Figure 19(b) is achieved when h is rather kept constant and the fiber probe tip moved across a surface. The fibre and light source properties as well as the reflecting material all affect these characteristic graphs.

The amount of output power received does not only depend on the receiving fibre end but also largely on the type and properties of the detector used.
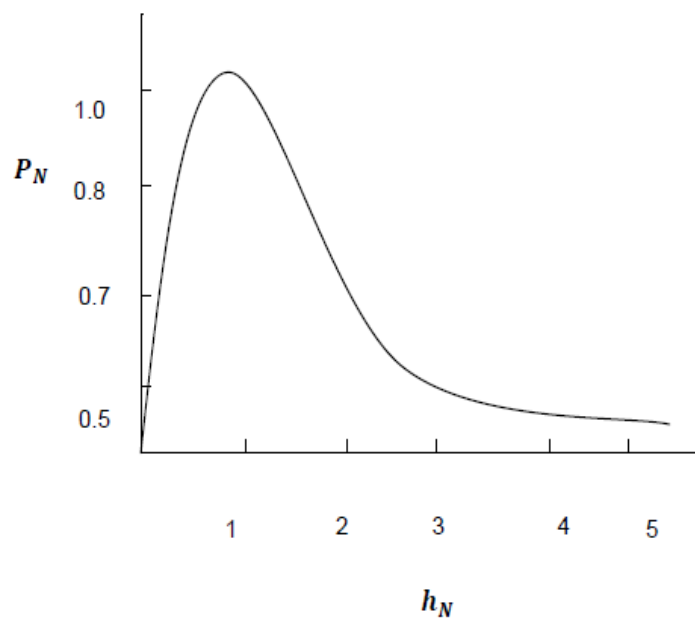
Figure 18: Transfer function characteristic curve representing normalized power P_N against normalized distance h_N obtained through the geometrical approach
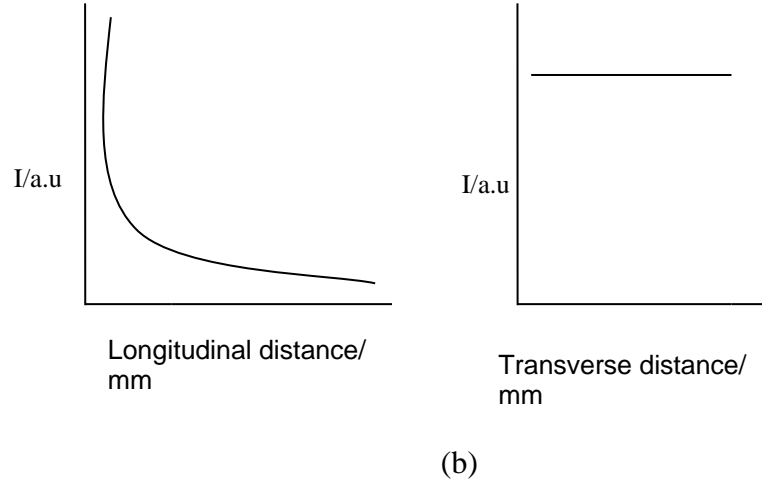
Figure 19: The characteristic graphs of the optical design depicting reflected

intensity against (a) longitudinal and (b) transverse distances

Two conflicting mechanisms take place as the longitudinal displacement (*h*)
increases. Firstly for small values of *h*, is the increasing of the effective
collecting area *S* as the fibre end (probe tip) gets progressively farther inside
the light cone and secondly, the decreasing of the irradiance *I* as the probe tip
collecting end moves away from the emitted light vertex when considering
higher values of *h*. In the analysis of the sensitivity of the design, the
derivative of the normalized power P_N is evaluated with respect to h_N.
Sensitivity of the optical design then becomes the minimum amount of light
that is detected within a specified range of displacement (Brandao, 1998).
Thus sensitivity *S* becomes:

$$S = \frac{\partial P_N}{\partial h_N} \tag{44}$$

Principles of Photodetection

Although light can be detected by the human eye, it is not suitable for use in modern optical systems because of slow response, poor sensitivity to low-level signals and difficulty in processing its information electronically. Furthermore, the spectral response of the eye is limited to wavelengths between 0.4 and 0.7 µm, where even fiber losses are high. This section looks at the basic principles of devices that directly convert optical signals to electrical signals (either current or voltage) and respond quickly to changes in the power level (Palais, 1992). In semiconductor junction devices free charge carriers (electrons and holes) are generated by absorption of incoming photon. This mechanism is sometimes called the internal photoelectric effect. Three common devices which use this phenomenon are *pn* junction photodiode, the PIN photodiode and the avalanche photodiode. Important detector properties are responsivity, spectral response, and the rise time. The responsivity ρ is the ratio of the output current i of the detector to its optic input power P. It is

$$\rho = \frac{i}{P} \tag{45}$$

The unit of responsivity is amperes per watt. In some detector configurations the electrical output is a voltage. In this case the responsivity is given in units of volts per watt of incident power. The spectral response refers to the curve of detector responsivity as a function of wavelength. Because of the rapid change in responsivity with wavelength within either of the windows of the optical spectrum, the responsivity at a specific wavelength emitted by the source must be used when designing the receiver. The rise time is the time

for detector output current to change from 10 to 90% of its final value when the optical input power is in step.

Semiconductor junction photodiodes are small, light, fast, sensitive and can operate with just a few bias volts. The simple *pn* photodiode, drawn in figure 20, illustrates the basic detection mechanism of a junction detector. When reverse biased, the potential energy barrier between the p and n regions increases. Free electrons (which normally reside in the n region) cannot climb the barrier, so no current flows. The junction refers to the region where barrier exists and because there are no free charges in the junction, it is called the depletion region or layer. Having no free charges, its resistance is high, resulting in almost all the voltage drop across the diode appearing across the junction itself. Hence electric forces are high in the depletion region and are negligible outside.
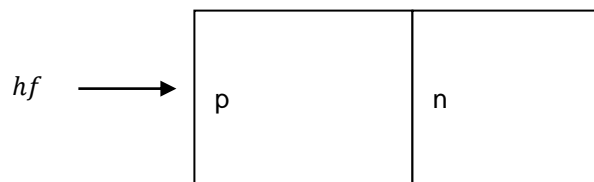
Figure 20: A pn junction

What happens when a photon is absorbed in the p or n regions outside the junction is that an electron hole pair is created. These free charges move slowly because of the weak electric forces outside of the junction. Most of the free charges diffuse through the diode and recombine before reaching the junction. These charges hence produce negligible current, thus reducing the detectors responsivity.

In figure 21, photons with energy hf greater than the bandgap W_g enter the semiconductor and are able to excite electrons from the valence band to the conduction band. If the electrons and holes produced reach the junction or are created within the depletion layer, they can be swept through the device and so generate a photocurrent. To liberate a single electron from the cathode requires a minimum amount of energy called the work function. Denoting the work function by $\emptyset$, the condition for release of an electron is thus

$$hf \geq \emptyset \tag{46}$$
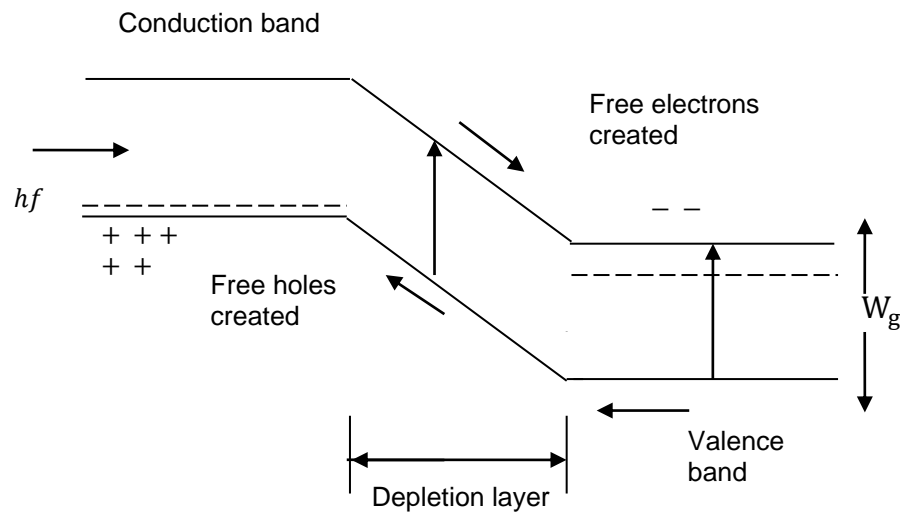
Figure 21: A semiconductor junction photodiode energy band diagram

The lowest optic frequency that can be detected is $f = \emptyset/h$. This corresponds to a wavelength of $\lambda = hc/\emptyset$. If the work function is given in electron volts, then the cutoff wavelength in (μm) becomes

$$\lambda = \frac{1.24}{\emptyset} \tag{47}$$

Wavelengths longer than this cannot be detected. However, not every photon whose energy is greater than the work function will liberate an

electron. The characteristic is described by the detector parameter called quantum efficiency η. This is defined by

$$\eta = \frac{\text{number of emitted electrons}}{\text{number of incident photons}}$$

Because the optic power is the energy per second being delivered to the detector and hf is the energy per photon, then P/hf is the number of photons incident on the cathode. With quantum efficiency η, the number of emitted electrons per second is then $\eta P/hf$. Since each electron carries charge of magnitude e, the charge per second (that is, the current) emerging from the cathode is

$$i = \frac{\eta e P}{hf} = \frac{\eta e \lambda P}{hc} \tag{48}$$

The definition strictly refers to the external quantum efficiency of the device, which takes into account losses due to reflection at the detector surface. The detector responsivity from equation (45) therefore is given by (Perlin, 1989)

$$\rho = \frac{i}{P} = \frac{\eta e}{hf} = \frac{\eta e \lambda}{hc} \tag{49}$$

Hence the output voltage is

$$v = \frac{\eta e P R}{hf} =$$

$$\rho P R_L \tag{50}$$

where current flows through the load resistor R_L in the external circuit.

The PIN diode has a wide intrinsic semiconductor layer between p and n regions, as illustrated in figure 22. The intrinsic layer has no free charges, so its resistance is high. Most of the diode voltage appears across it and the electrical forces within are also strong. Because the intrinsic layer is

very wide, there is a high probability that incoming photons will be absorbed in it rather than in the thin p or n regions. This improves the efficiency and the speed relative to the pn photodiode.
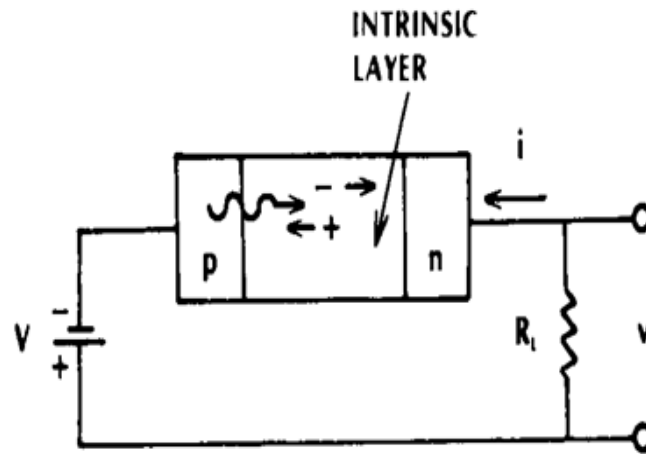
Figure 22: PIN photodiode in the reverse-bais (Palais, 1992).

To achieve very good external quantum efficiency, carrier recombination is highly avoided thus minimizing photon absorption outside the depletion layer. This depends on the device design. Absorption within the depletion layer is maximized when $H \approx 2/\alpha - 3/\alpha$, where α is the coefficient of absorption. Most importantly, reflection from the detector surface must as well be reduced by using antireflection coating.

CHAPTER THREE

EXPERIMENTAL APPARATUS AND PROCEDURES

In this work, light intensity was used to sense small displacements of objects from a reference point. The optical system seeks to examine material surfaces by measuring micro displacement of the target which is a reflective surface using light from a bifurcated optical fibre. Light is incident at one arm serving as the input arm of the fibre and the back reflected light after striking a target (reflective surface) goes through the other arm termed as the output arm which is connected to a detecting system for measurements to be recorded.

Apparatus Description

Light sources

In this work three different light sources were used. A uniphase D-8152 He-Ne laser of wavelength 633 nm with beam diameter of 1 mm and a guaranteed 4 mW minimum output power which generates a continuous wave was used. This laser produces a high optical quality light with a TEM_{00} Gaussian output profile. The laser housing has an adapter head which allows other accessories to be attached. The other two sources are incorporated in a single system. This system is an FIS OV-LS dual light emitting diode (LED) source which emits an 850 nm and 1310 nm wavelengths. The rated optical power for both wavelengths is -17 dBm (20.0 μW) which is very typical. The spectral bandwidth also typically is 45 nm at 850 nm and measures 170 nm at

1310 nm. It must also be stated that the temperature range of operation for this light source is $+ 14^0$ to 122^0F (-10^0 to $+50^0$C). Depending on which wavelength one wants to operate, the SELECT SOURCE knob is pressed and a red light indicates on either source 1 or 2. Each source has an output port to aid connection to other accessories. For a continuous wave emission, the CW MODE button is pressed. The FIS OV-LS is powered by a 9 V DC regulated power supply which was built in this work order to get a stable delivery of power from the emitting light source.
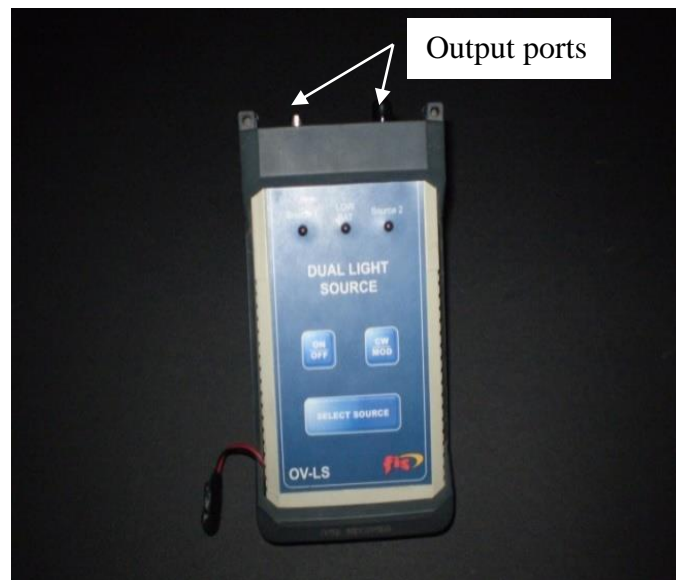
Plate 1:   The FIS OV-LS

The Probing Fibre

The optical fibre probe consist of a glass bifurcated multimode optical fiber cable of diameter (100/140 μm). The cable combines the input and the output arms into one assembly, in a random mix at the sensing point (fibre probe tip) and cylindrically housed in a brass case. It is an ideal configuration

for application that requires a compact sensing tip. The 100 μm core, 140 μm cladding diameter graded index multimode optical fibre has a numerical aperture (NA) of 0.29 ± 0.015 and attenuates at less than 4.0 dB/Km at 850 nm and less than 1.5 dB/Km for 1300 nm. The sensing point of the fibre operates with an active diameter of 50 μm. It has a robust and easy to use connectorize ends.
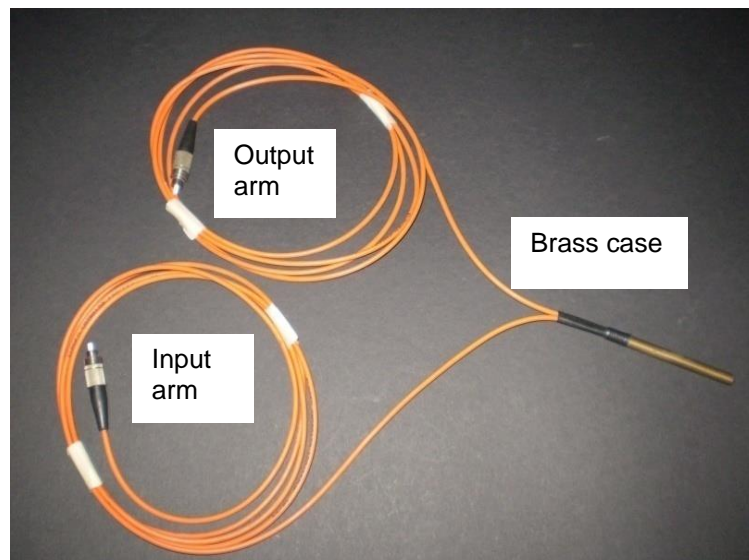
Plate 2: The bifurcated multimode fibre used in the experiment

Photodiode (818-Sl)

The detector used was a silicon photodiode 818-Sl from Newport Company. It is housed in a cylindrical structure. The (818-SL) detector is actively sensitive to visible region detection even though it has a spectral range of 400 nm to 1100 nm. It uses the finest large-area, planar-diffused PIN silicon in its operation. Thus, its operation is generated by voltage across a p-n junction of a semiconductor. It is optimized for zero-bias operation to provide the low noise, high stability and uniformity in measurements. With an average

power maximum-W/o attenuator of 2 mW/cm^2, the accuracy at constant temperature is $\pm$ 2% at 400 nm-1100 nm having an active area and diameter of 1 cm^2 and 1.13 cm respectively.
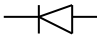
Plate 3:   A cylindrical 818-Sl detector

Metex M-3850D

This digital multimeter was manufactured and tested in accordance with IEC 1010 and DIN57411/VDE0411 part safety requirement for electronic measuring apparatus, safety class II by Geprutte Sicherheit in Germany. This is an analogue to digital converter. This instrument does not measure voltages greater than 1000 volts DC or 750 volts AC. It is also operated on a 9 V DC power supply. This avoids voltage drops which may heather to result in erroneous readings. Table 1 provides limit on inputs in order to ensure the safety working of this instrument to avoid damage when in use.

Table 1: Input Limits

FUNCTION	TERMINAL	INPUT LIMIT	
V DC	V/Ω + COM	1000V	DC
V AC	V/Ω + COM	750V	AC
Ω	V/Ω + COM	250V	DC/AC
m/A DC/AC	mA + COM	400mA	DC/AC
20A DC/AC	20 A + COM	20A	DC/AC
▷|	V/Ω + COM	250V	DC/AC
Freq.	V/Ω + COM	750V	DC/AC
Logic	V/Ω + COM	250V	DC/AC

By pressing the top-left red button, the instrument turns ON or OFF. To select a function, the rotary is switched to the appropriate switch position and the instrument is ready for normal operation. The back-lit display is operated by pressing the yellow button. It automatically turns off in seconds. There is also the SET/RESET button which can be pressed to enter, and then pressed again to exit. By automatically turning off the power extends to the life of the power supply if neither the rotary switch nor push button is operated for 10 minutes.

Plate 4:   M-3850 D Metex instrument with its connecting cable

FIS OV-PM

This FIS OV-PM optical power meter devise has an easy to read LCD display. This detector has a 2 mm germanium PIN photodiode with a dynamic range of 70 dB (+ 5 dBm to -65 dBm). Independent zero set function for each of the two available wavelengths conveniently allows storage of unique zero reference levels. The unit goes into the sleep mode if no keypad strikes are detected within 25 minutes and may reactivate by simply pressing the ON/OFF key. One important feature of this optical power meter is the rugged solid-rubber holster which provides protection for performance durability. By pressing the wavelength (λ) button, a selection of the particular wavelength to be detected is made. The available detection wavelengths are 850 nm, 1310 nm and 1550 nm. Measurements are recorded in units of either dB or dBm and the selection is aided by the press of the dB/dBm button. This comes along with the FIS OV-LS dual light source system to ease the output readout of the power.

Plate 5: The FIS OV-PM optical power meter

The Regulated 9 Volt (DC) power supply

The DC power supply was designed to produce a stable output voltage of 9 V and was purposely built to stabilize the mains voltage, thereby eliminating battery voltage drops which could affect measurements. It has a special feature of an external battery terminal which allows connection to a 12 V battery and subsequently gives out 9 V equivalent power supply for field work. The regulator switch allows selection between the mains and the external terminal whereas the toggle switch makes ON and OFF selection. The components used in the construction included the following: 9 V transformers (at 1.1 A), quick blow fuse (1 A), and a bridge rectifier. There was also the 470 μm electrolytic capacitor, a 100 μm electrolytic capacitor, time delay fuse (160mA), a toggle switch, pilot lamp, I C regulator, an insulating enclosure, slide switch, flush panel fuse holders and some wires. The circuit diagram was designed and transposed onto the Printer Circuit Board (PCB) and was etched in a concentrated hydrochloric acid for about three hours. It was then removed,

allowed to dry and cleaned. With the aid of a designed circuitry the various components were fixed by soldering. A heat sink was also incorporated into the system to conduct excess heat away. The completed circuit board was placed in a $12 \times 12 \times 8$ cm insulation enclosure and covered. The power supply was tested by plugging its cable into a mains socket and the input terminal to a 230 V variac (shown with an arrow in plate 6) which varied the input voltage from 228 to 175 V and an Agilent Technologies oscilloscope (DS06012A) which monitored the input a.c transformer secondary voltage, output regulated and unregulated d.c voltage signals. Measurements were recorded as voltmeter readings for regulated and unregulated d.c voltages.
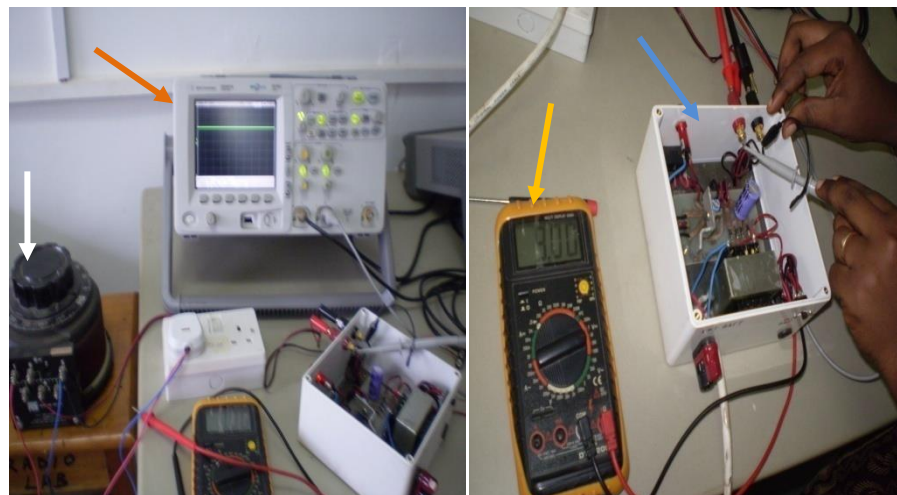
Plate 6: The opened power supply (blue arrow) connecting to the Variac (white arrow), DS06012A oscilloscope (orange arrow) and the voltmeter (yellow)
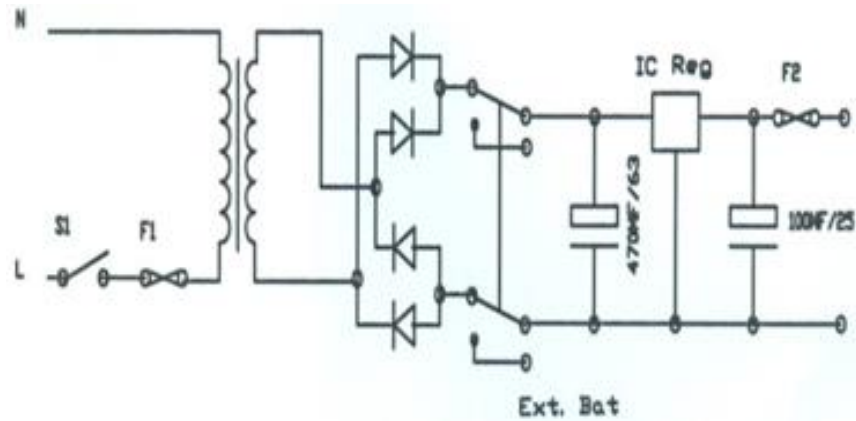
Figure 23: The circuitry diagram for the 9 V d.c regulated power supply

Samples

A round protected silver mirror (PF10-03-P01) of diameter 25.4 mm and 6.0 mm thickness from Thorlabs was the standard mirror used. Other samples used in the experiment included a BK 7 rectangular glass block of diameter 4 cm by 2.5 cm by 0.8 cm, a clear glass ground edge microscope slide (CAT. NO. 7105) of 25.4 mm by 76.2 mm and thickness of 1.2 mm dimension from Sail Brand 10 (China) was also obtained from the School of Biological Sciences Laboratory. Adding to these samples were the Sony 700 MB CD-R and CD-WR (4x-24x high speed) which were both filled with 349.9 MB of data. A non galvanized hot-rolled steel plate of thickness 0.6 mm was also cut into a size of 3.5 cm x 4.0 cm. this was obtained from Sethi Brothers Ghana limited (Tema). A polished aluminium plate from Aluworks Ghana limited which was composed of 99.7% of pure aluminium was cut into a size of 3.8 cm x 2 cm (1mm thick).

Some paracetamol tablets were also used. These are locally manufactured tablets which were obtained from the sales agent of the two manufacturing companies in Cape Coast (Nat and Sons Pharmacy). The Letap

and the M/G tablets are products of the Letap pharmaceutical and M&G pharmaceuticals Company limited respectively. These tablets were separately examined due to their relatively small size and for that matter small surface area within which measurement were taken. Two different types of the Letap were used. The differences came from their dates of manufacturing, expiration and sizes. Tablets categorized under Letap A both had a diameter of 12.1 mm and thickness of 4.7 mm and were manufactured in May 2007 and expired in March 2010 and come from one sachet under the label letapA1 and letapA2. Letap B comprises three different tablets from the same sachet labeled as Letap B1, B2 and B3, was manufactured in July 2009 and expires in July 2012. For the M/G, there was only one sachet (six tablets) of a sample which was manufactured in June 2009 and expires in July 2014. It was ensured that sample surfaces had no visible defect.

Experimental setup

In this work, the laser source (D-8152 He-Ne) was focused through a microscope objective (MO) lens of focal length 0.25 cm from Melles Griot into one arm of the bifurcated multimode optical fibre probe which was used as the input arm. The light travels along the length of the input arm of the fibre until it illuminates the surface of the plane mirror (PF10-03-P01). The microscope objective lens and the sample were separately and respectively mounted on translation stages (XYZ) to enable fine alignment so that a high percentage of the laser light was coupled into the input arm of the fibre. The emerging light was incident at 90° (normal incidence) on the mirror surface. Due to the reflective nature of the mirror, the light is reflected back almost in

the same direction of the incident beam and is randomly mixed. The light thus goes through the other arm designated as output arm of the fibre probe. At any stage it was ensured that the offset gap between the fibre probe tip (sensing area) and the mirror surface was about the thickness of a standard A4 paper (210 x 297) mm which was determined to be 0.1 mm. The reflected intensity of the light is detected by the 818-SL photodiode which was connected to the Metex instrument and data was read and recorded in terms of voltage.

Two types of measurements were done on the plane mirror sample first, in the transverse direction and secondly in the longitudinal direction. The mirror was made to move away (longitudinal distance) from the fibre probe tip for a distance of 20 mm in intervals of 0.5 mm with the aid of translation stage and then back to its original position. Two reflected intensity recordings were done to ensure good sample positioning.

A second method was used to track possible defects by transversing the sample along the path of the incident light at fixed minimum distance. Here, the mirror was moved across the fibre probe tip to give a transverse scan of the sample surface at 0.5 mm interval and the offset gap of 0.1 mm was maintained. Sample surfaces were scanned at different positions of 1 mm vertical displacement and normalized intensities plotted. The area of scan line per point was (0.5×1) mm^2 and for each sample the scanning was repeated three times and the mean of the measurand (reflectance) evaluated. Using the same experimental approach, the surfaces of the various tablets were also transversely scanned within the displacement range of 4.6 mm. Figure 24 and plate 7 depicts the experimental setting used in this work.
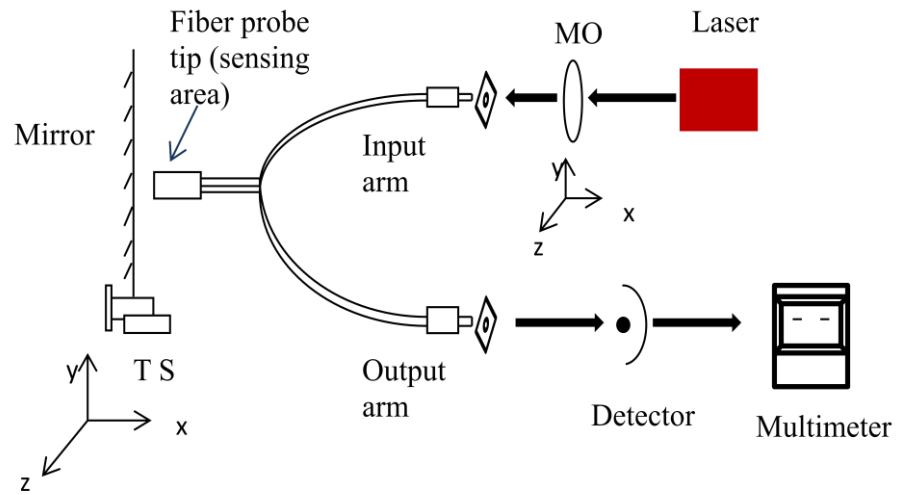
Figure 24: A sketch of the experimental setup
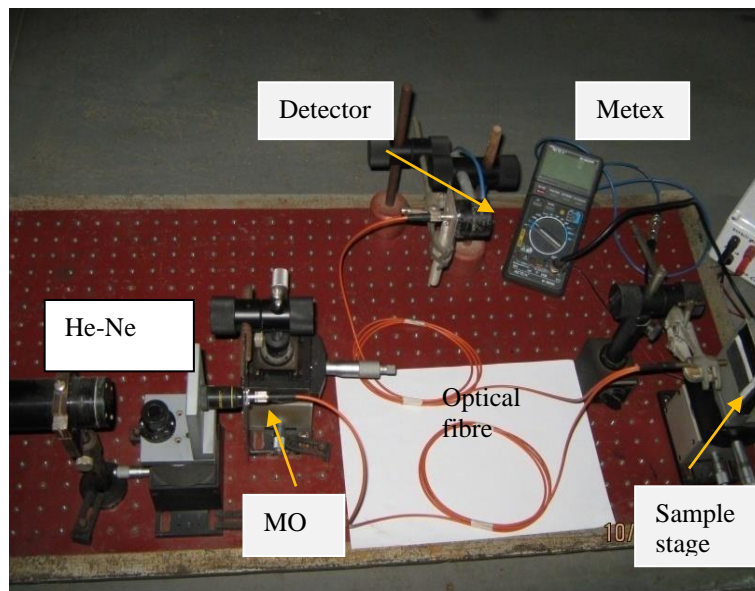

Plate7: The experimental setup showing the He-Ne laser, the microscope

objective lens (MO), the bifurcated optical fibre , the sample stage,

detector (818-SL) , and the Metex multimeter instrument (M-3850D)

The experimental procedure was repeated using two other light sources which were both emitted by the FIS OV-LS system. In this setup the connectorize ends of the bifurcated fibre were connected directly to the FIS OV-LS and the FIS OV-PM with the input arm connected to the 850 nm source output port whiles the output arm went to the FIS OV-PM power meter. By this connection, coupling losses were terminated. Recordings were made from the power meter by selecting the required wavelength. The fibre input arm end was detached and connected into the 1310 nm port whiles maintaining the output arm connection. Measurements were taken for each of the samples.

Due to multimode connector tolerances, the sharp point of an angled ferrule may crack the lens of many 850 nm LED source and cause erroneous readings. Therefore an angled-physical contact (APC) connector was installed into the 850 nm light source output port. (Giotta & Salamone, 1990)
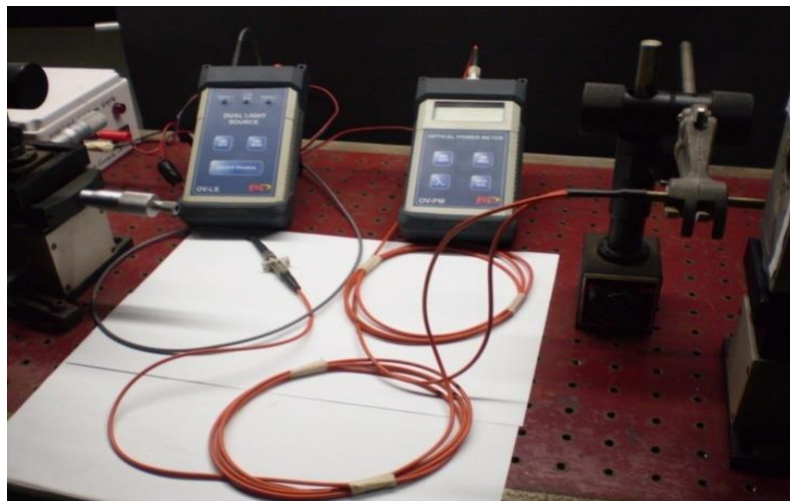
Plate 8: Set-up showing the connection of the FIS OV-LS, FIS OV-PM, bifurcated optical fibre probe and the sample stage

53

Beam diameter verification

A verification of the laser beam diameter was conducted using the knife edge method. Here, a single-edged razor blade was attached to a micrometer driven translation stage to eclipse the laser beam. The intensity of the uneclipsed portion of the beam was measured with a detector. The experimental data was obtained by moving the translator and blade in small increments to gradually allow less and less of the laser beam to strike the detector, thus effectively eclipsing the beam with the blade. The points in the beam where the energy or power is 90% and 10% of the total respectively are used to calculate the Gaussian beam radius.

Figure 25: Setup for the beam diameter verification

CHAPTER FOUR

RESULTS AND DISCUSSION

This chapter presents the results obtained from the work done. The first section shows results from the transverse displacement of the sample from the fibre probe tip. The next section shows resul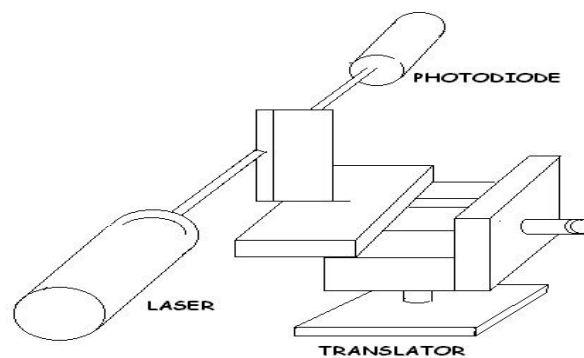ts obtained from the longitudinal displacement of the samples. The third section exclusively presents results on the transverse displacement of some locally manufactured paracetamol tablets. The fourth and final section contains a detailed analysis and discussion of the results. In this work, the reflectances of materials were examined using three light sources of different wavelengths.

The surface reflectance (R) using transverse displacement

From the definition of reflectance in chapter two, at normal incident of light to a sample surface a resulting reflectance value can be obtained. The reflectance for the various samples were obtained in the transverse displacement of each sample using the three light sources as described in chapter three. In all, 10 figures comprising the transverse reflectance measurements and the normalized longitudinal reflectance measurements are presented.

Figure 26: A graph of average reflectance against transverse displacement of the plane mirror using the three light sources. The reflectance values for 850 and 1310 nm LED sources are approximately the same
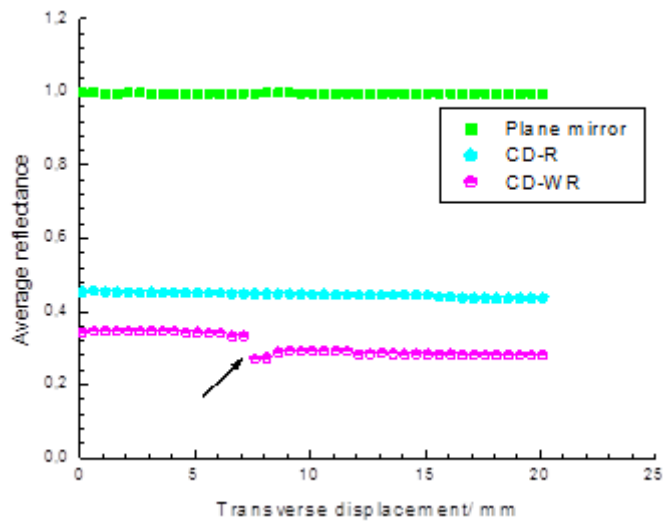
(a)
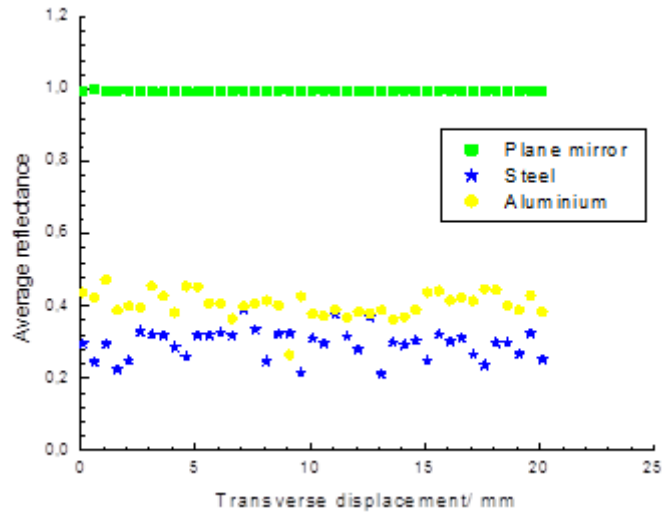
(b)
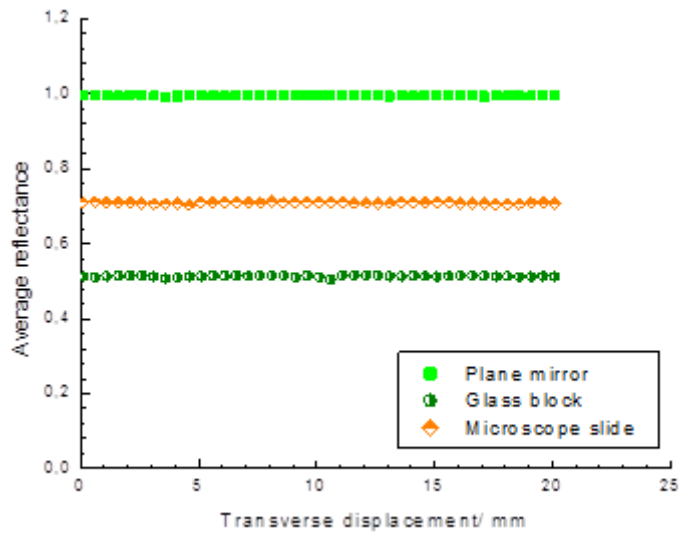
(c)

Figure 27: Graphs of average reflectance against transverse displacement for
(a) Plane mirror, CD-R and CD-WR (b) Plane mirror, Steel and Al
and (c) Plane mirror, Glass block and Microscope slide using the
850 nm LED source

(a)

(b)

(c)

Figure 28: Graphs of average reflectance against transverse displacement for (a) Plane mirror, CD-R and CD-WR (b) Plane mirror, Steel and Al and (c) Plane mirror, Glass block and Microscope slide for the 1310 nm LED source
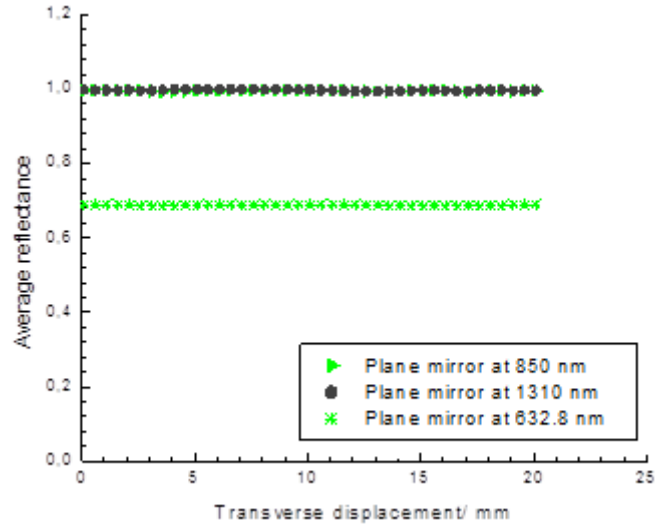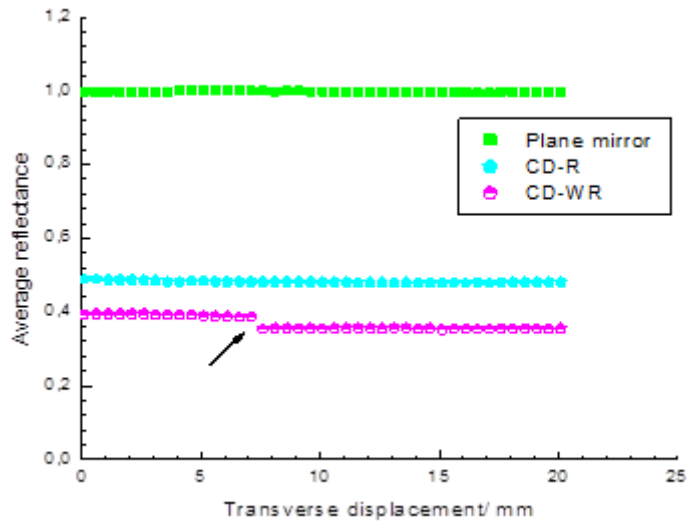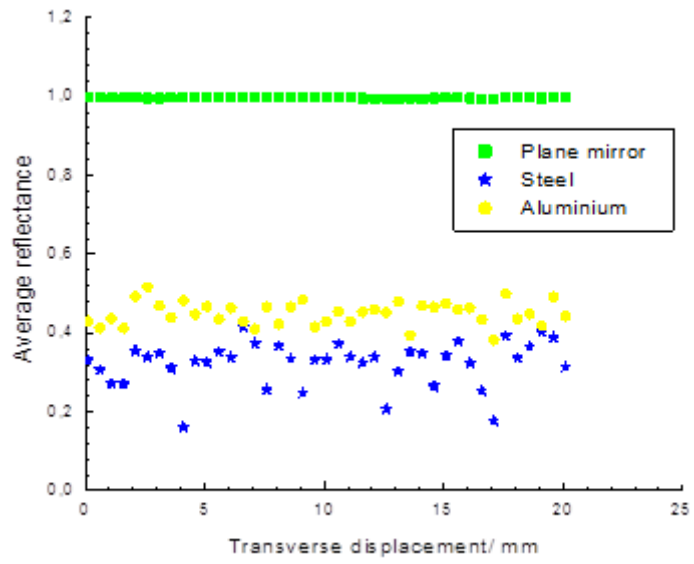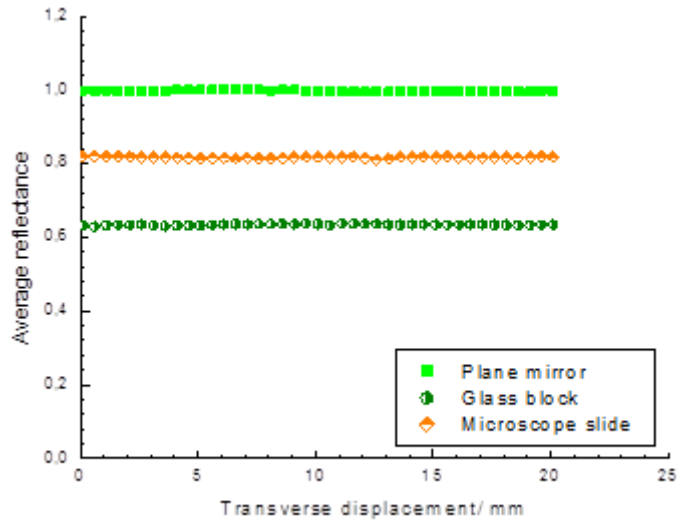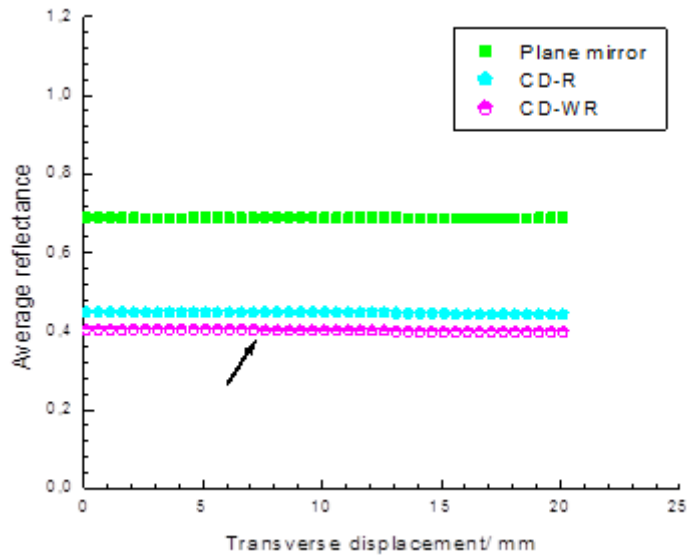

(a)
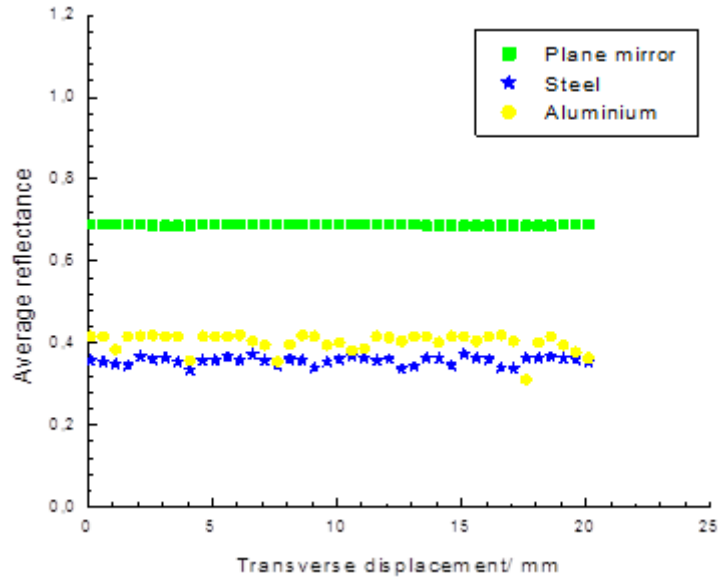
(b)
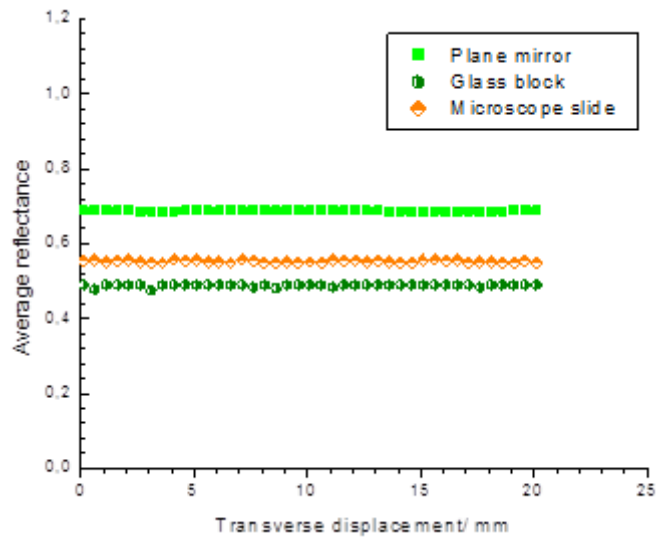
(c)

Figure 29: Graphs of average reflectance against transverse displacement for (a) Plane mirror, CD-R and CD-WR (b) Plane mirror, Steel and Al and (c) Plane mirror, Glass block and Microscope slide for the 632.8 nm LED source

Table 2 gives the respective resulting average reflectance of seven of the samples obtained using the definition of reflectance given on page 24 of chapter two of this thesis. From the definition, the incident intensities of the various sources at the fibre probe tip were determined as follows: the 632.8 nm He-Ne laser was 0.341 V, 850 nm LED had 33.96 dB and 39.62 dB for 1310 nm.

The reflected intensities were the recorded intensities from the receiving end of the fibre to the detector which was recorded as voltage readings on the Metex instrument for the He-Ne laser and on the FIS-OV-PM power meter in decibels (dB) for the other two LED sources. From table 2, the plane mirror which was used as the standard sample proved to have the best reflectivity of approximately 70% of the 632.8 nm He-Ne laser, 99.5% of the 850 nm and 99.7% of the 1310 nm LED sources respectively. The corresponding reflectance values of the plane mirror were almost unity which means that the plane mirror reflected almost 100 % of the light from the 850 and 1310 nm LED sources and the values were very close thus an over-lap in the plotted results shown in figure 26.

Table 2:   Average reflectance of the various samples for the three light
sources   used

Samples	Average reflectance from the three light source wavelength		
	632.8 nm He-Ne	850 nm LED	1310 nm LED
Plane mirror (PF10-03-P01)	0.68907	0.99592	0.99739
Glass block	0.48855	0.51469	0.63426
Microscope slide	0.55225	0.71109	0.81676

Steel plate	0.35684	0.29657	0.32291
Aluminum plate	0.40233	0.40584	0.44982
CD-R(Sony 700MB)	0.44689	0.44760	0.48213
CD-WR(Sony 700 MB 4x-24x high speed)	0.30699	0.36854	0.40176

It could also be seen from table 2 that five of the samples showed increasing average reflectance with increasing wavelength. Only two samples thus the steel plate and the CD-RW did not follow an increasing trend. This could be attributed to an inherent property of the material. The average reflectance of the steel plate for the 632.8 nm laser was rather higher than for the 850 and 1310 nm light source. It showed a much lower average reflectance and it displayed a profile similar to an irregular surface texture as seen in figures 27(b), 28(b) and 29(b). Graphs in figure 27(a), 28(a) and 29(a) showed that across the scanned length i.e. (moving from empty region to where there is information or data on the CDs), there was a sharp decrease (indicated on the graphs with arrows) especially with the CD-WR in average reflectance and this change in reflectance varied depending on the wavelength of light source used. Even though the aluminum had a better reflectance than the steel it also showed some level of surface irregularities. In the graphs of figures 27(c), 28(c) and 29(c), the reflectance of the microscope slide was higher than that of the glass block for all three light sources.

Results obtained from the longitudinal displacement of the seven samples.

In figure 30, within the normalized displacement range of 0.1 to 7.0 the optical system could best detect (maximum sensitivity) the reflected light from the mirror. The response of the optical sensing design remained approximately linear with an error of ± 0.0001 within the operating displacement range of 0.1 to 7.26 as shown in figure (30b). For larger displacement movements, the rest position (which is the point at which detector sensitivity is minimum) of the mirror was 47.76 and 51.95 for the 850 nm and 1310 nm light sources respectively. The minimum sensitivity point of the mirror when the He-Ne laser was used was 40.99. From these points within the normalized reflected range of [40.0; 56.0], the sensing response also remained approximately constant. It could therefore be said that, since the operating point for minimum sensitivity corresponds to a higher reflected intensity which relates to a higher optical power level for that matter, it therefore means that operation of the optical design could be observed with less noise-sensitivity which may be advantage.

(a)

63
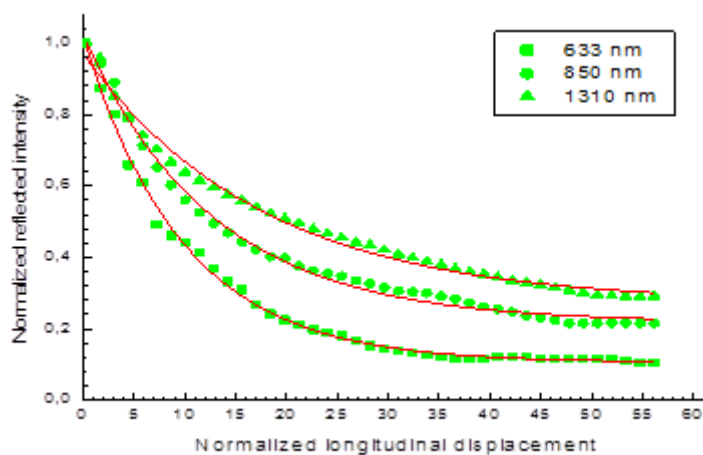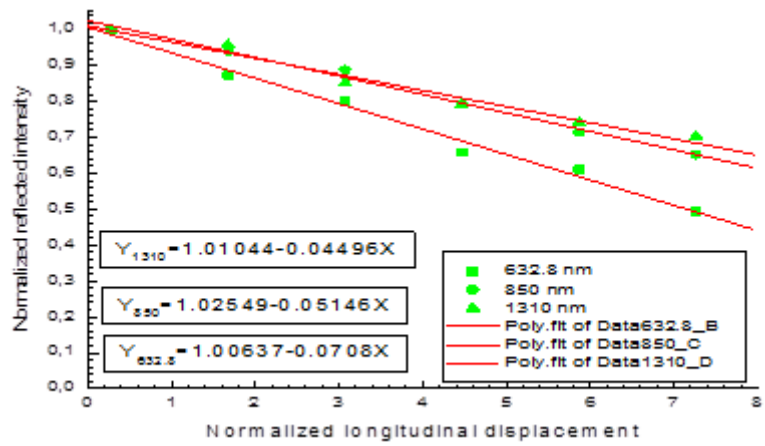
(b)

Figure 30: A graph of normalized reflected intensity against normalized longitudinal displacement of the plane mirror using 632.8 nm, 850 nm and 1310 nm light sources

(a)

(b)
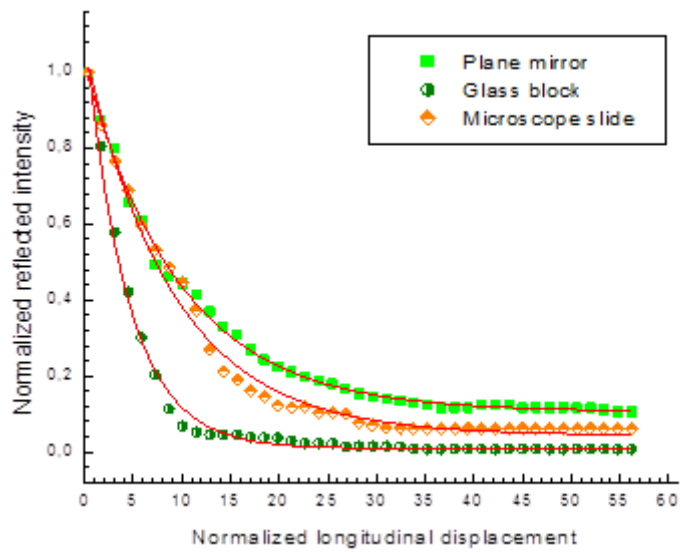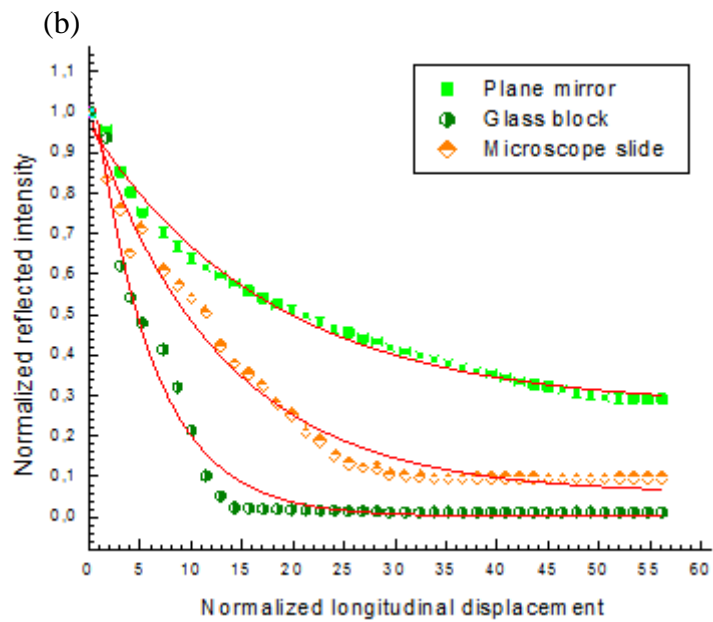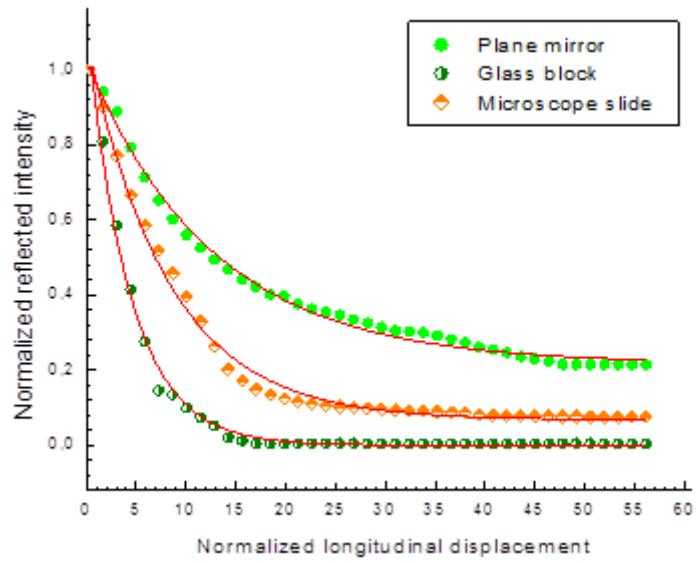
(c)

Figure 31: Graphs of normalized reflected intensity against normalized longitudinal displacement for the Plane mirror, Glass block and Microscope slide   using (a) 632.8 nm He-Ne laser (b) 850 nm LED and (c) 1310 nm LED
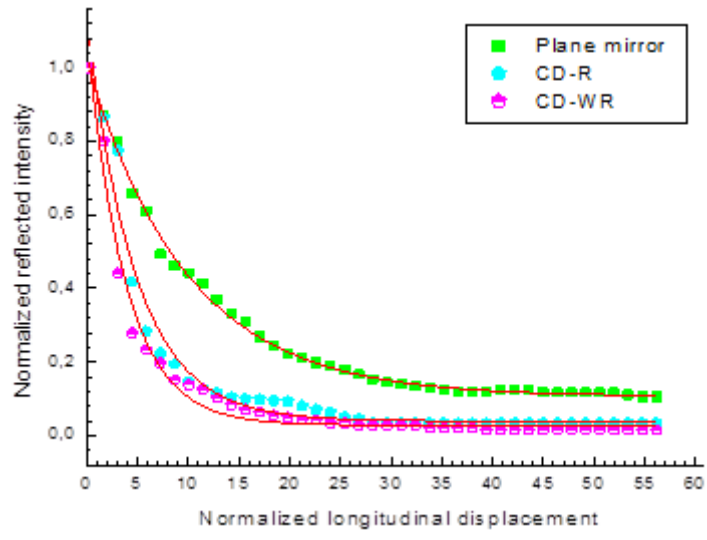
(a)
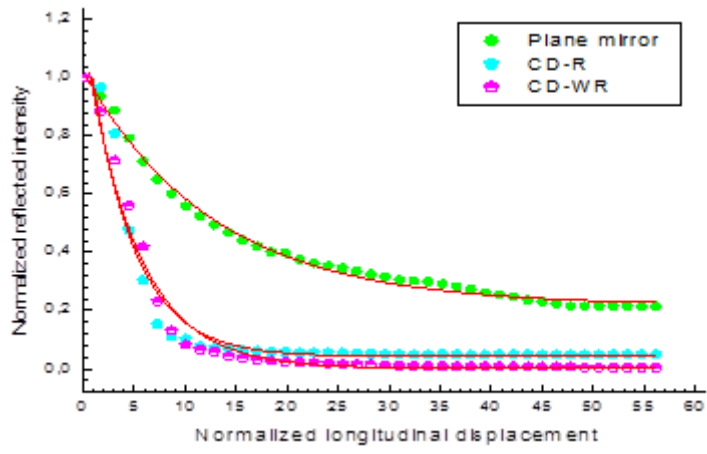
(b)
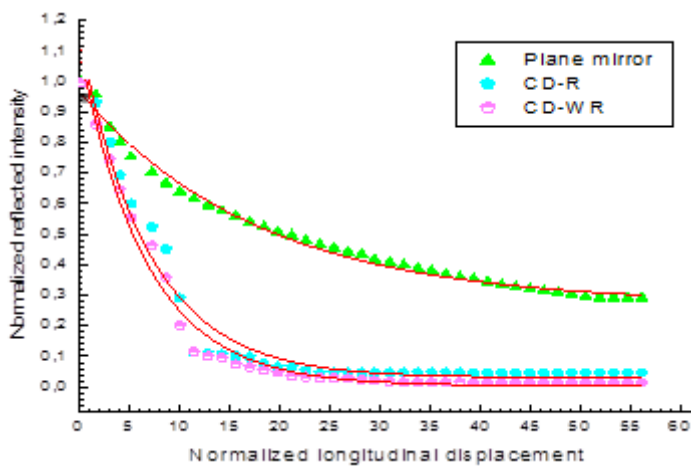
(c)

Figure 32: Graphs of normalized reflected intensity against normalized longitudinal displacement for the Plane mirror, CD-R and CD-WR using (a) 632.8 nm He- Ne laser (b) 850 nm LED and (c) 1310 nm LED
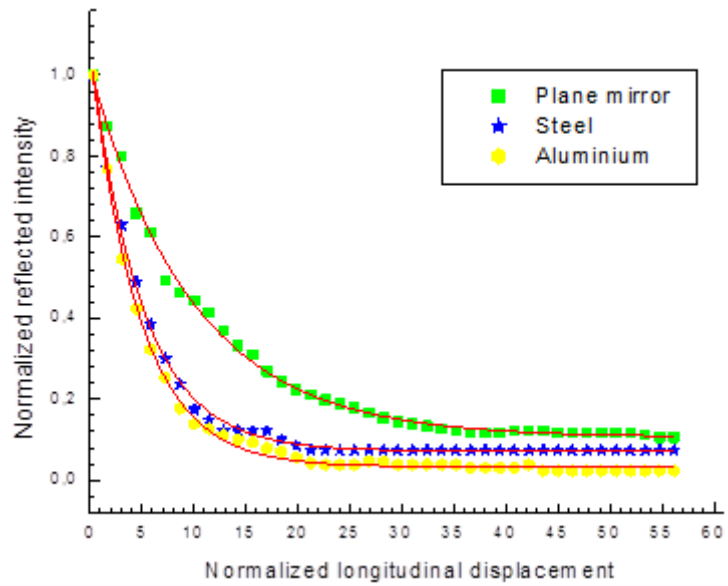
(a)
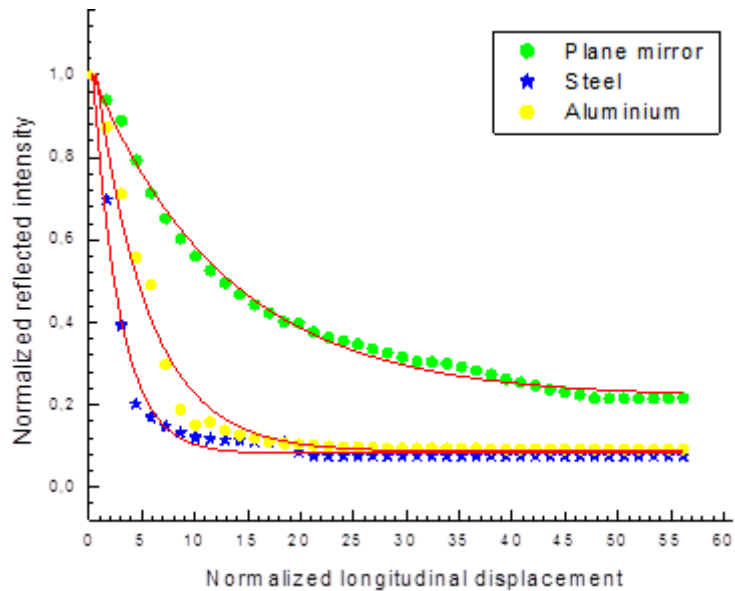
(b)
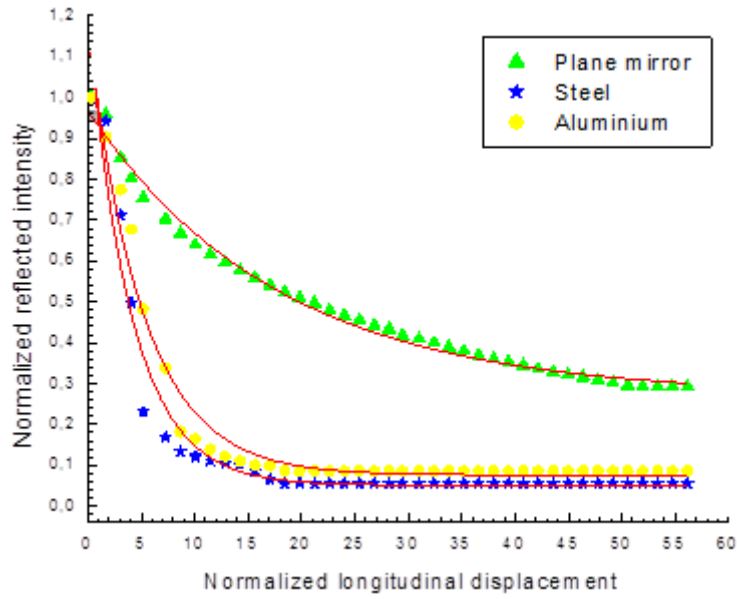
(c)

Figure 33: Graphs of normalized intensity against normalized longitudinal displacement for the Plane mirror, Steel and Al using (a)632.8 nm He-Ne laser (b)850 nm LED and (c) 1310 nm LED

From the graphs shown in figures 30 to 33, it could be observed that the reflected light intensity from the surface of the object under investigation decreased rapidly with distance from the fibre probe tip. Hence the optical sensing system did not completely vary linearly with displacement. For longitudinal displacement values higher than those used in the graphs, the asymptotic decline (attenuation) continued and no change was observed to that effect after the depth point (range for minimum sensitivity). Within the range of longitudinal displacement values used, intensity falls as $\frac{1}{\zeta^2}$ for increasing displacement values. At such higher longitudinal displacement h, the divergence angle of the emitting light is extended beyond its regular size which tends to minimize the acceptance angle of the receiving end as discussed in chapter two of this thesis.

From the results shown in graphs obtained in figures 30 to 33, it could be deduced that the optical design for sensing could detect (maximum sensitivity) most of the samples placed within the range of 0.1 to approximately 7.0 with reasonable linearity for the three light sources used except the microscope slide whose maximum sensitivity was within the range of 0.1 to 13.0. It could also be realized that exponential decay in the glass block was steepest in all three light source wavelengths in comparison to the plane mirror which had the best reflectance especially in the 1310 nm light source. This is established in graphs of figure 30 especially in (c). Here, the resting positions of the glass block and microscope slide for higher displacement differed slightly in both 632.8 nm and 850 nm but the 1310 nm light source gave a rest position of 35.0 for the microscope slide. In figure 32, the CD-R and CD-WR proved to have a resting position at 39.0 within the normalized displacement range of [37.0; 56.0]. Also, the glass block, CD-R and CD-WR within their range of rest had very low reflected intensities. In figure 33, although the steel and aluminium plates had their rest positions at 20.0, it was also evident that they rather had higher normalized reflected intensity within the range of rest [20.0; 56.0] and this was higher than that of the CDs and the glass block. The details of the fittings of the curves in figure 31, 32 and 33 are elaborated in table 3.

Equation (45) was used in fitting the curves in figures 30 to 33.

$$y = y_0 + A_1 e^{-x/t_1} \tag{45}$$

where, x is the varied parameter (longitudinal displacement), y_0 the off-set or point at which decay becomes constant or nearly parallel to the horizontal axis. A_1 represents the amplitude or the initial intensity of the light whose reduction is determined by the factor e^{-x/t_1} and is approximately 1 for all samples according to the exponential fit which agrees with the starting normalized reflected intensity. The t_1 is the decay constant which depends on the properties of the material surface such as the surface coating, finish, and texture. This was observed to be higher for samples with higher reflectance values.

Table 3(a): Values of equation parameters for the 632.8 nm He-Ne laser

Samples at 632.8 nm	R^2	y_0	A_1	t_1
Plane mirror	0.99698	0.10604	0.91252	9.80262
Microscope slide	0.99080	0.04370	1.01350	9.12658
Glass block	0.99343	0.00860	1.10500	4.30428
CD-R	0.97411	0.03943	1.09376	4.77416
CD-WR	0.98232	0.02782	1.06317	3.79896
Aluminium	0.99746	0.03304	1.02651	4.68307
Steel	0.99783	0.07162	0.99344	4.92761

Table 3(b): Values of equation parameters for 850 nm LED.

Samples at 850nm	R^2	y_0	A_1	t_1
Plane mirror	0.99358	0.21825	0.80433	12.75620
Microscope slide	0.99251	0.067251	1.01365	8.11508
Glass block	0.99369	0.00078	1.11844	4.27410
CD-R	0.95460	0.04236	1.17542	4.32400
CD-WR	0.97897	0.00155	1.15623	3.06690
Aluminium	0.98077	0.04236	1.04401	4.97830
Steel	0.98771	0.08194	1.04906	2.58250

Table 3(c): Values of equation parameters for 1310 nm LED

Samples at 1310 nm	R^2	y_0	A_1	t_1
Plane mirror	0.99006	0.27340	0.90619	17.65290
Microscope slide	0.98287	0.05670	0.94397	12.72610
Glass block	0.97788	0.00014	1.12544	6.79832
CD-R	0.96817	0.02869	1.12488	6.92685
CD-WR	0.98135	0.00222	1.11241	6.66851
Aluminium	0.96679	0.07464	1.08833	5.11325
Steel	0.96667	0.04994	1.13686	4.05605

Results obtained from the paracetamol tablets.

The graphs in figure 34 show the reflectance variation across the set of pharmaceutical tablets for Letap A and B. The reflectance was lower in the case of the Letap A tablets. The average reflectance values for the three light sources are tabulated in table 4.
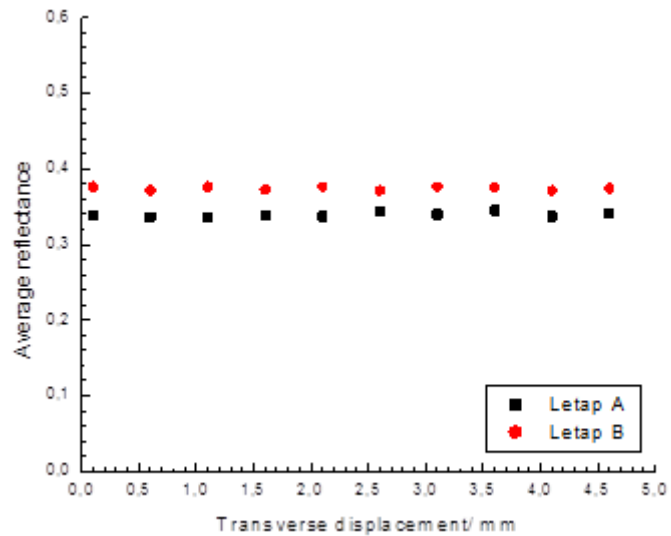
(a)
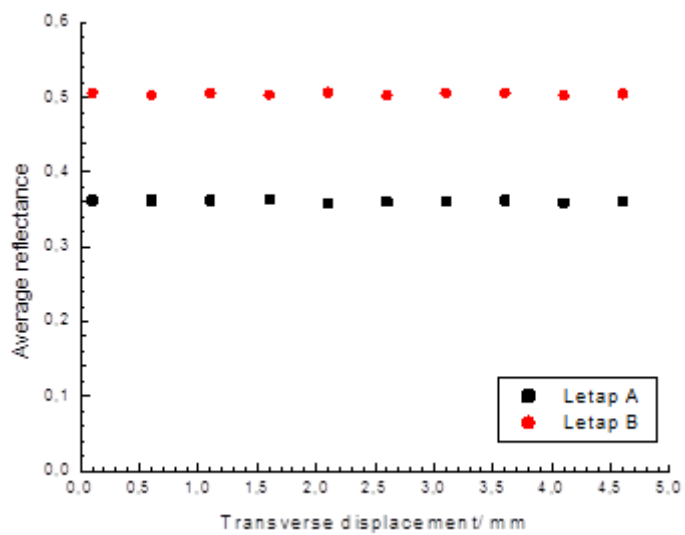
(b)
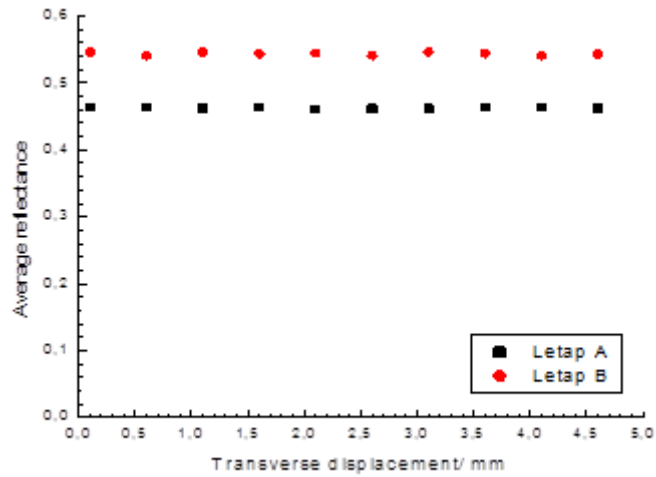
(c)

Figure 34: Graphs of average reflectance against transverse displacement of Letap A and B sets of tablets using (a) 632.8 nm He-Ne Laser (b) 850 nm LED and (c) 1310 nm LED light sources
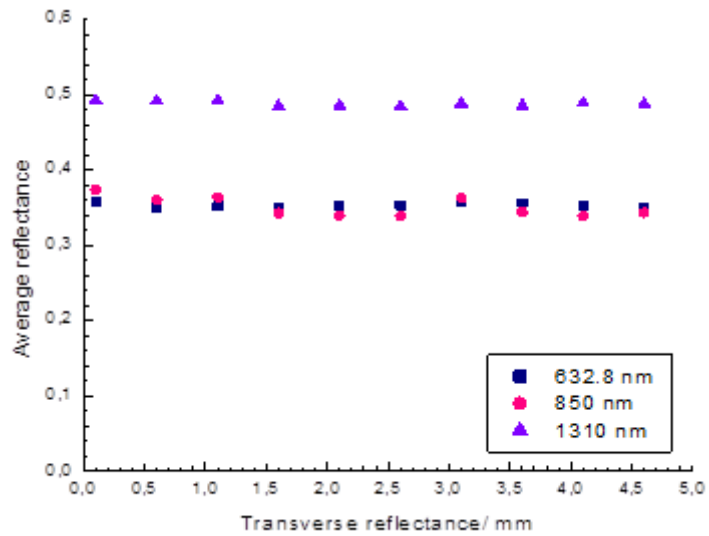
Figure 35: A Graph of average reflectance against transverse displacement of the six tablets from one M/G sachet using the 632.8 nm He-Ne laser, 850 nm and 1310 nm LEDs

73

Table 4: Average reflectance values of the tablets of Letap A, B and M/G for the three light sources

Tablet samples	Average reflectance from the three light source wavelength		
	632.8 nm	850 nm	1310 nm
Letap A (Expired)	0.33936	0.37419	0.46273
Letap B (Unexpired)	0.36129	0.50484	0.54402
M/G	0.35298	0.35728	0.48809

The graph in figure 35 gives the results obtained from the M/G tablets. It could be observed from figure 34 and 35 that the paracetamol tablets from visual inspection were of white colour and recorded very low reflectance in comparison to the plane mirror. This was due to some diffuse scattering from the surface of the tablets. These scattering could not be eliminated due to the short length of the off- set distance between the fiber probe tip and the tablet surface. The incident intensity of 15.57 dB and 5.22 dB for the 1310 nm and 850 nm LED sources respectively gave average reflectance values of 0.488094 and 0.357287. The laser (He-Ne) had an incident intensity of 0.341 V and gave an average reflectance value of 0.352981 for the M/G tablets. The graphs also showed the surface profile patterns of the tablets. The results confirmed the repeatability of the optical design for sensing as results from each tablet for a particular light source proved to be similar after surface was scanned three times.

The beam diameter verification

From the knife edge method discussed in chapter three the subsequent calculations were done to confirm the diameter of the 632.8 nm He-Ne laser beam since it was necessary in the choice of the scan length and area of the various sample surfaces. Since the beam radius is defined as the radius where the intensity is reduced to $1/e^2$ of the value at r = 0 and by letting r = w_L from the equation of the Gaussian spatial distribution that is: $I(r) = I_0 e^{\left(-2r^2\middle|w_L{}^2\right)}$, the diameter of the beam can be calculated (Koshrofian et al., 1963).

From the graph in figure 36, the beam diameter was therefore evaluated to be 1.0529 ± 0.0018 mm which is the Gaussian beam diameter of the 632.8 nm He-Ne laser used in this work.
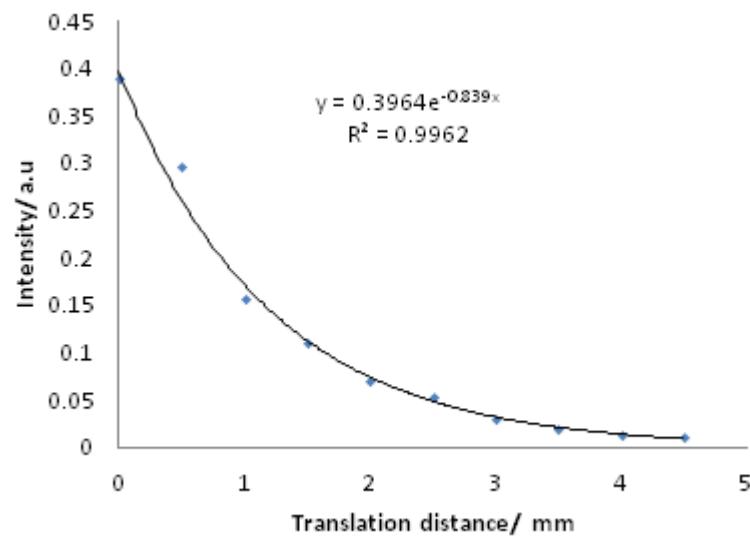
Figure 36: The resulting graph of output intensity against translation distances of the razor blade using the 632.8 nm He-Ne laser

The 9 V regulated power supply

The construction of this power supply was to replace the battery or the dry cell which had voltage drops over a long period of usage. Series of tests were done after it was constructed to ensure that its accuracy and efficiency guarantees an effective user result. The obtained results in table 4 are the various voltage readings when the 9 V power supply was connected to a 230 V varaic (variable voltage transformer).

Table 5: Various measured a.c voltages at the transformer output and input as well as the regulated and unregulated d.c voltages

A.C Mains Voltage / V	A.C.Transformer secondary voltage/ V	Unregulated D.C Voltage/ V	Regulated D.C Voltage/ V
228	9.85	12.20	9.00
215	9.30	11.39	9.00
210	9.12	11.18	9.00
205	8.91	10.89	9.00
200	8.68	10.56	9.00
195	8.52	10.31	8.99
190	8.29	10.01	8.98
185	8.11	9.76	8.78
180	7.89	9.44	8.46
175	7.64	9.12	8.15

From table 5, it could be noticed that the effective output regulated d.c voltage remained steadily constant at 9.00 V for the higher transformer voltages (228 to 200 V) after which it started dropping since voltage was getting really low as shown in figure 37 (a) and this was as expected since the power supply was to produce a stabilized 9 V output d.c voltage of the mains voltage. However, a plot of the mains voltage against the unregulated d.c voltages gave the resulting graph in figure 37(b) which showed a linear fit within the range of mains voltages used. It was also observed that the amplitude of the d.c unregulated voltage was higher than the regulated voltage as monitored by the oscilloscope. This is due to the fact that the transformer's a.c output voltage is specified at the full-load current–off load and so the voltage rises in accordance with the regulation specified for 9 V transformer in the power supply (Stifter, 1997).
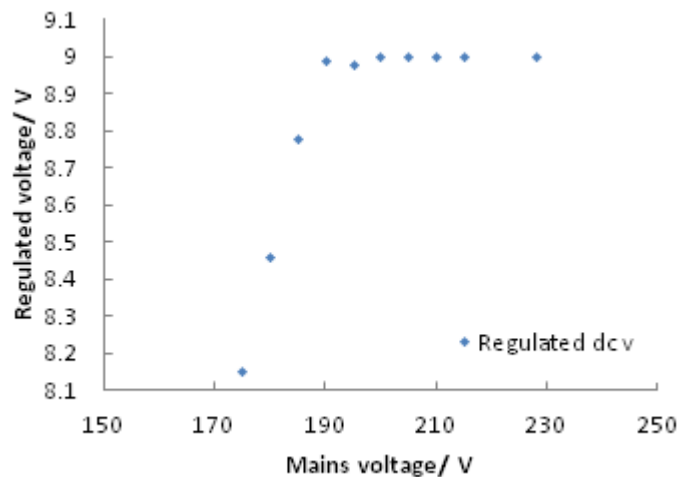
(a)
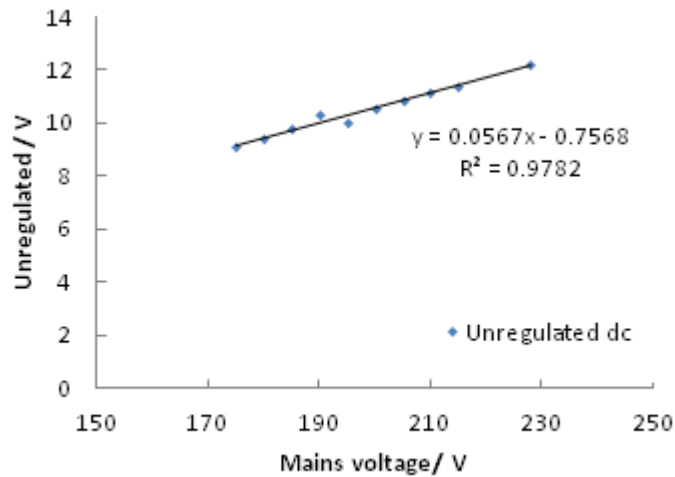
(b)

Figure 37: Voltage graphs of (a) Regulated d.c voltage (b)Unregulated d.c

voltages against the mains voltage

Discussion

From the detailed results shown in the previous section, the results

obtained in the transverse displacement of all the samples clearly shows that

the reflected intensities at any given point on the surface are closely related to

the reflectance properties of the respective samples (Nayar et al., 1991).

The plane mirror had a better reflectance value for all the light sources.

Since silver is of very good reflectivity within the optical region used in this

work (Hecht, 2008). On the other hand, the reflectance value at 632.8 nm was

very low approximately 70% as against the expected value of 97% according

to the material's property by the manufactures (Thorlabs incorporated). This is

due to increasing scattering in a shorter wavelength of light source (Giotto &

Salamone, 1990). This could be attributed to the value of the beam diameter

1.0529 ± 0.0018 mm obtained in this experiment which differed slightly from

the supposed value of 1.0 mm.

In most metals, free delocalized electrons travel with a velocity derived from the average field from the source. This results in Feynman's low-frequency approximations where the metal is considered as opaque; both the real and imaginary parts of the refractive index are assumed to be of equal magnitude. Since the atoms are a small portion of wavelength of light, countless number of atoms and electrons are excited and re-radiate energy (reflection) near the metal surface (Feynman et al., 1964). From the graphs in figure 33, the decay near the metal surfaces causes both a rapid decrease in the intensity of the light and creates a big phase shift in the excitation and the reflection from the free electrons. Maxwell's wave equations which were discussed in chapter two therefore require that the reflected field should be equal to the incident wave in magnitude and only be 180° out of phase so that the vector sum of the intensities of the incoming wave and the outgoing wave at the surface is zero (an effective short circuit) which is a condition for surface reflection at normal incidence (Leighton et al., 1964). Even though the unpolished steel did not have 100% reflectivity, it could be seen that its reflectivity in the 632.8 nm was the highest (0.356841) amongst the three light sources. This is because it has a large imaginary part of its refractive index thus making it a good absorber. However, for any good absorber at any frequency the general rule is that light waves are strongly reflected at the surface and very little is absorbed (Leighton et al., 1964). Metals therefore could be said to reflect visible light well. The aluminum metal however, differed a little from this point since its surface was coated with a polishing or shinny material whose composition (0.03%) may have enhanced the surface

reflection and hence the slightly higher reflectance values for the 850 and the 1310 nm LED sources.

Reflection in the glass block is however different, the incident of an electric field of the source on the atoms of the transparent material generates a field which is related to the source field. This field appears to move at a different speed inside the glass and the corresponding charges are also reflected from the back to the front. This backward going field is the one we see reflected from the surfaces of transparent materials especially glass. Reflected light does not come only from its surface. The backward reflection comes from everywhere in the interior, but it turns out that the total effect is equivalent to a reflection from the surface (Raymond, 2001).

Reflectance values (from figures 27(c), 28(c) and 29(c)) in the microscope slide were higher as compared to the rectangular glass block (BK7). Since the rectangular glass block was thicker it is possible the backward reflections take a longer time to arrive at the surface and subsequently to the receiving fibre. This time delay may result in the dispersion of the light in time and hence absorption occurs. Moreover, since refractive index is wavelength dependent (Saleh &Teich, 1991), it could therefore be deduced from the reflectance relation in equation (34) of chapter two that reflectance is higher in the microscope slide which is made of borosilicate glass with refractive index 1.53 than reflectance values of the glass block whose refractive index is 1.51. In the infrared region the microscope slide had an approximate reflectivity of (81%) within the limits of the experimental errors.

Both the recordable (CD-R) and re-writeable (CD-WR) compact discs are composed of polycarbonate layers coated with a reflective layer sandwiched between a substrate and a lacquer surface. The CD-WR surface is normally a metallic layer made of aluminum but sometimes aluminum alloy is stamped with microscopic pits, arranged in a continuous spiral grooves which guides the light beam incident on it. Results obtained from graphs in figure 27(a), 28(a) and 29(a) clearly depict that reflectance of CD-R are higher than that of the CD-WR. This is due to the presence of a highly optimized special dye layer coated on the CD-R surface (Kees & Schouhammer, 1998). This organic dye is a phthalocyanine which is usually made of silver or gold, is chemically stable and also has a relatively better reflectivity both in the visible and infrared wavelengths in comparison to the aluminum coating in CD-WR. Moreover, the moderately photosensitive or non-reactive layer (dye) however, gave an abrupt change in reflectance and this was more pronounced in the CD-WR, indicating an empty region from a data recorded region. That is, the recorded data in a CD is stored in tiny indentations (pits). These are encoded in the tightly packed spiral track molded into the top of the polycarbonate layer. Since pit is approximately 100 nm deep by 500 nm wide, and varies from 850 nm to 3.5 μm in length, by incidenting a light beam on the polycarbonate layer, the changes in height between the pits and "lands" results in the difference in intensity of the light reflected (Janes et al., 1997). This intensity difference is however modified by the grooves in the empty regions on the disc and hence the high reflected intensity difference values. For this reason, it is even advised that CDs are carefully handled as scratch can also cause a data recording or reading problems (Pohlmann, 1992).

The paracetamol tablets though with less percentage reflectivity in comparison to the silvered mirror displayed an important phenomenon. It was evident that Letap A tablets were of lower reflectivity and this may be due to the fact that they have stayed longer on the shelf. The M/G tablets showed approximately same reflectance values for a particular light source which gives the evidence that constituents of tablets in one sachet from a particular pharmaceutical firm may have same optical properties. The difference in surface reflection profiles between the Letap and M/G tablets may results from the differences in the various coating substances used especially. This result also justifies the difference between white and shiny surfaces. Since there is a degree of surface roughness in the white coloured paracetamol tablets in comparison to the shinny surfaces of the glass block, microscope slide and plane mirror.

CHAPTER FIVE

CONCLUSION AND RECOMMENDATION

Conclusion

The interaction of light with matter can be characterized by sensing an optical property of the material called reflectance. This uses reflection from the material surface. Such approach was adopted by using three light sources of different wavelengths to examine the surfaces of eight different samples. The technique employed by this reflectance system (optical design) showed that each surface has a unique reflectance value and this varied with wavelength. The mean reflectance of the eight samples which included a plane mirror, rectangular glass block, clear microscope slide, aluminium plate, steel plate, Sony 700 MB CD-R, Sony 700 MB CD-WR(4x-24x high speed), a set of Letap and M/G paracetamol tablets were investigated. The analyses of the experimental results on reflectance which were evaluated are shown in table 6.

From the results, the highest reflectance value was obtained from the plane mirror in all three light source wavelength giving a proof of its high surface quality in terms of smoothness and hence making it a good choice for a standard sample. The reflectance values of the selected samples depend on the nature of the surface of the material. The system could also provide surface profile data and dependence of reflectance on wavelength of light source. The repeatability of the optical design was also established as tablets from a particular sachet proved to have approximately same reflectance within a

common light source wavelength. Reflectance characteristics of old and newly manufactured tablets could be used to give qualitative properties of the tablets. The optical design and technique used in this work could be a tool for tablet identification as well as testing tablet quality. The non-contact optical design or surface sensing based on reflection was able to measure reflectance within the chosen longitudinal displacement range and showed that intensity falls with distance which could obey the inverse square law. However, the system could not respond to small changes in reflectance at very large longitudinal displacement range. This therefore establishes the dependence of the optical power or intensity collected by the receiving end of the fiber probe tip on the variable longitudinal displacement (h).

Table 6: Summary of results

Samples	Reflectance from the various wavelength of Light sources		
	632.8 nm He-Ne	850 nm LED	1310 nm LED
Plane silvered mirror (PF10-03-P01)	0.68981	0.99592	0.99739
Glass block	0.48845	0.51469	0.63426
Microscope slide	0.55225	0.71109	0.81677
Aluminum plate	0.40233	0.40584	0.44982
Steel plate	0.35684	0.29657	0.32291
Sony CD-WR	0.30699	0.36854	0.40176
Sony CD-R	0.44689	0.44760	0.48213
Letap A Expired	0.33933	0.33741	0.46273
Letap B Unexpired	0.36129	0.50484	0.54402
M/G	0.35298	0.35728	0.48809

Recommendation for future work

It is recommended that the following should be considered in future work. The system should be automated for usefulness in a number of industrial and forensic applications. The frequency-domain approach which is the Fourier transform of the time domain can be used to investigate the results of modulating the intensity of the light source.

Additional light sources made up of LEDs could be employed to give reflectance surface spectra and minimize cost in reflectance surface spectroscopy.

REFERENCES

Adams, M. J. (1981). *Introduction to optical waveguide*. John Wiley & Sons Inc., 2nd ed., 2 - 5.

Bekefi, G. & Barete, A. H. (1977). Electrmagnetic radiations, waves and vibrations. MIT Press 321.

Boyles, W. (1994). *Instrumentation reference book.* Amazon, 3rd ed., 172 - 175.

Byrne, G., Dornfeld, D., Inasaki, I., Ketteler, G., Konig, W. & Teti, R. (1995). Tool Condition Monitoring (TCM): the Status of research and industrial application. Anals of the CIRP, 44/2, 541 - 562.

Brandao, F. J. (1998). IEEE Transaction on instrument and measurement: a theoretical analysis of the bifurcated fibre bundle displacement sensor. **47**, No 3, 742 - 747.

Bradly, C. & Jeswiet, J. (1999). An optical surface texture tensor suitable for integration into a coordinate measuring machine. Anals of the CIRP, **48/1/1999**, 459 - 462.

Culshaw, B. & Dakin, J. (1989). *Optical fibre sensors*: *principles and components*. Artech, Boston, **1**, 28 - 44.

Feynman, R. P., Leighton, R. B. & Sands, M. (1964). The Feynman lectures on physics: reflection from surfaces. Addison - Wesley. **2**, Chapter 33

Guenther, R. (1990). *Modern Optics*. Wiley, Canada. 26 - 30 and 62 - 78.

Ghatak, A .K. & Shenoy, M. R. (1994). *Fibre optic through experiment*. Viva books, India, 3 - 5.

Giallorenzi, T. G. , Bucaro, J. A., Dandridge, A. Sigel, *G. H.* Jr., Cole, J. H.

    Rashleigh, S. C. & Priest, R. G. (1982*). Optical Fibre Sensor*

    Technology. IEEE J. Quantum. Electrodynamics, QE-18, 626.

Giotta, F., & Salamone, D. (1990): *Fibre Optic Lab Manual: Communication*

    Fibre Optics. 3rd ed., Fibre Instrument Sales, Inc., New York, 54 - 58.

Hecht, E. (2002). *Optics: International edition*. Adison Wesley, San

    Francisco, 4th ed., 36 and 48 - 50.

Hecht, E. (1989). *Optics,* 2nd ed. Adison Wesley, Toronto, 100 - 102.

Hecht, J. (2008). *Understanding Lasers*. IEEE Understanding Science and

    Technology Series, Wiley, New Jersey, 3rd ed., 46 - 47 and 310.

Janes, H., Du, G. & Stuart, P. (1997). Doing cultural studies: the story of the

    sony walkman. Thousand Oaks, California, SAGE Publications.

Jerkins, F. A. & White, H. E. (1976). *Fundamentals of Optics*. McGraw-Hill,

    New York, 4th ed., 24.

Kees, A. & Schouhamer, I. (1998). *The CD Story.* Journal of the AES 46,

    458 - 465. Retrieved on February 9, 2010.

    www.exp-math.uni-essen.de/immink/pdf/cdstory.html

Klein, M. V. & Furtak, T. E. (1996). *Optics.* Wiley, Canada, 2nd ed., 59 - 85.

Koshrofian, M. J., Garetz, B. A., & Jordan, E.C. (1963). Measurement of

    gaussian beam diameter. applied optics, **28**, Issue 9, 907.

Leighton, R., B., Feynman, R., P., & Sands, M. (1964). The Feynman Lectures

    on Physics. Refractive Index of Dense Materials. Addison-Wesley, **2**,

    Chapter 32.

Lin, G.C., Shea, T., & Hoang, K. (1977). Measurement of surface roughness with a laser beam. Australian conference on manufacturing engineering. 132 - 133.

Liu, Z., Wang, A., Yue, X., C., Wang, Y., Wang, Q., & Cai, X. (2001). "Distributed Optical Fibre Temperature Detecting and Alarm System." 12th International Conference on Automatic Fire Detection, Gaithersburg, USA.

Miltcho, D., Mills, J. N. & Demidovich, A. (2004). *Fibre optic kit: introductory experiments*. ICS UNIDO, 6 - 8.

Nayar, S. K., Ikeuchi, K. & Kanade, T. (1991). Reflectance: geometrical and physical perspectives. IEEE transactions on pattern analysis and machine intelligence, **13**, No. 7, 611 - 632.

North, W.P.T. & Agarwal, A. K. (1983). Surface roughness measurement with fibre optics. Technical brief, ASME journal of dynamic systems, measurement and control, **105**, 295 - 297.

Palais, J. C. (1992). *Fibre Optic Communications*. Prentice, New Jersey, 3rd ed., 167 - 173 and 70 - 75.

Perlin, A. R. (1989). Single optical fibre transducers: a technical overview on the subject. Interopto '89 Int, optoelectronic exhibition. (Tokyo).

Pohlmann, K. C. (1992). *The Compact Disc Handbook*. Middleton. Wisconsin, A-R Editions.

Raymond, M. (2001). *Structural Monitoring with Fibre Optic Technology*. Academic press, San Diego, Califonia, U.S.A. Chapter 7, 401 - 406.

Rideout, D. (2009). Understanding surface metrology tools. Retrieved on January 23, 2010. www.physics.ponoma.edu/course/phys

Smith, F. G. & Thompson, J. H. (1988). *Optics*. Wiley, New York, 2nd ed., 48 - 55.

Stifter, F. J., Natick, Massechusett. Retrieved on November 29, 2009. http:// www.elect-spec.com

Salei, B.E.A. & Teich, M.C. (1991). *Fundamentals of Photonics*. Wiley, Canada, 3rd ed., 177.

Spurgeon, D. & Slater, R.A.C. (1974). In-Process indication of surface roughness using a fibre optic transducer. 15th International Machine Tool Design and Research, **15**, 339 - 347.

Siegman, A. (1986). *Lasers*. Mill Valley, CA, University Science.

Tyndall, J. (1854). History of total internal reflection. Retrieved on November 8, 2009. http://schools.wikia.com/wiki/Total_Internal_Reflection

Wang, J. L. J., & Kusiak, A. (2001). *Computational intelligence in manufacturing handbook*. Amazon, **2000**.

Yeh, C. (1989). *Hand book of fibre optics: theory and applications*. San Diego, Califonia, 286 - 295.